nature geoscience

ARTICLES

https://doi.org/10.1038/s41561-021-00846-6

Check for updates

Direct astronomical influence on abrupt climate variability

Xu Zhang[1,2,3]✉, Stephen Barker[4], Gregor Knorr[3], Gerrit Lohmann[3,5], Russell Drysdale[6], Youbin Sun[7], David Hodell[8] and Fahu Chen[1,2]

Changes in the magnitude of millennial-scale climate variability (MCV) during the Late Pleistocene occur as a function of changing background climate state over tens of thousands of years, an indirect consequence of slowly varying incoming solar radiation associated with changes in Earth's orbit. However, whether astronomical forcing can stimulate MCV directly (without a change in the background state) remains to be determined. Here we use a comprehensive fully coupled climate model to demonstrate that orbitally driven insolation changes alone can give rise to spontaneous millennial-scale climate oscillations under intermediate glacial conditions. Our results demonstrate that an abrupt transition from warm interstadial to cold stadial conditions can be triggered directly by a precession-controlled increase in low-latitude boreal summer insolation and/or an obliquity-controlled decrease in high-latitude mean annual insolation, by modulating North Atlantic low-latitude hydroclimate and/or high-latitude sea ice–ocean–atmosphere interactions, respectively. Furthermore, contrasting insolation effects over the tropical versus subpolar North Atlantic, exerted by obliquity or precession, result in an oscillatory climate regime, even within an otherwise stable climate. With additional sensitivity experiments under different glacial–interglacial climate backgrounds, we synthesize a coherent theoretical framework for climate stability, elaborating the direct and indirect (dual) control by Earth's orbital cycles on millennial-scale climate variability during the Pleistocene.

Glacial–interglacial (G-IG) cycles were the primary feature of Earth's climate during the Pleistocene and occurred with periodicities linked to changes in Earth's orbit[1,2]. Co-evolving with these G-IG cycles was millennial-scale climate variability (MCV)[3–7], also known as Dansgaard–Oeschger (DO) cycles in Greenland ice cores from the last glacial period[8]. These large and repeating millennial-scale oscillations between stadial and interstadial conditions have been associated with changes in the mode of the Atlantic Meridional Overturning Circulation (AMOC)[9–13]. Because its occurrence extends back to at least 800,000 years before present (ka) in the ice-core record[14], MCV has been acknowledged as a ubiquitous feature of glacial climate[5,7,14]. Earth's orbit, as the fundamental external driver of the climate system[1], has also left its imprints in MCV. For example, the magnitude of the MCV features evident periodicities related to Earth's precession, obliquity and eccentricity[15–18] (Fig. 1a–c). This link has been proposed to be related to the dependence of MCV on G-IG changes in the climate background state (that is, ice volume and greenhouse gas concentrations) (Fig. 1d)[4], which is also supported by the robust coherent ~100-kyr periodicity between millennial-scale activity and Earth's orbit (Fig. 1c). The associated dynamics have been widely investigated by fully coupled climate models and synthesized using a conceptual framework of AMOC nonlinearity/bistability[9,10,12,19]. We refer to this as the indirect role of orbital changes on MCV. Meanwhile, the clear coherent periodicities of ~21 kyr and 40 kyr (Fig. 1c) motivated us to ask whether changes in the orbital configuration might give rise to MCV directly, for example, by modulating the strength and/or mode of the AMOC, especially during intermediate glacial periods when climate boundary conditions are relatively stable in comparison to transitions between glacial and interglacial states (that is, a direct role). The potential importance of this role has been tentatively explored using conceptual and simple dynamical system models[20,21]. However, the results are inconclusive due to a lack of support from fully coupled climate models that include more advanced climate physics.

Using an atmosphere–ocean fully coupled climate model, we aim to assess whether insolation changes alone can give rise to changes in the state of the AMOC that resemble DO events. Because different internal climate components (for example, atmospheric CO_2, ice volume and ocean circulation) are tightly interconnected[22–24], it is important to identify an appropriate time interval in which the occurrences of MCV can be attributed to insolation changes alone. Based on available proxy records[25,26], we selected a period during the later stage of marine isotope stage (MIS) 3 (40–32 ka), during which DO events 5 to 7 occurred in succession and apparently were not greatly influenced by changes in ice volume and atmospheric CO_2. Note that we do not aim to reproduce these recorded DOs by varying the full boundary conditions during this period, but instead aim to employ them as a surrogate for a systematic and generic understanding of AMOC responses to changes in Earth's orbit under intermediate glacial conditions. With the aid of transient and equilibrium experiments, we confirm that orbital changes alone can directly account for the occurrences of MCV.

[1]Group of Alpine Paleoecology and Human Adaptation (ALPHA), State Key Laboratory of Tibetan Plateau Earth System, Resources and Environment (TPESRE), Institute of Tibetan Plateau Research, Chinese Academy of Sciences, Beijing, China. [2]Key Laboratory of Western China's Environmental Systems (Ministry of Education), College of Earth and Environmental Science, Lanzhou University, Lanzhou, China. [3]Alfred Wegener Institute Helmholtz Center for Polar and Marine Research, Bremerhaven, Germany. [4]School of Earth and Ocean Sciences, Cardiff University, Cardiff, UK. [5]MARUM-Center for Marine Environmental Sciences, University of Bremen, Bremen, Germany. [6]School of Geography, Earth and Atmospheric Sciences, The University of Melbourne, Parkville, Victoria, Australia. [7]State Key Laboratory of Loess and Quaternary Geology, CAS Center for Excellence in Quaternary Geology and Global changes, Institute of Earth Environment, Chinese Academy of Sciences, Xi'an, China. [8]Godwin Laboratory for Paleoclimate Research, Department of Earth Sciences, University of Cambridge, Cambridge, UK. ✉e-mail: xu.zhang@itpcas.ac.cn

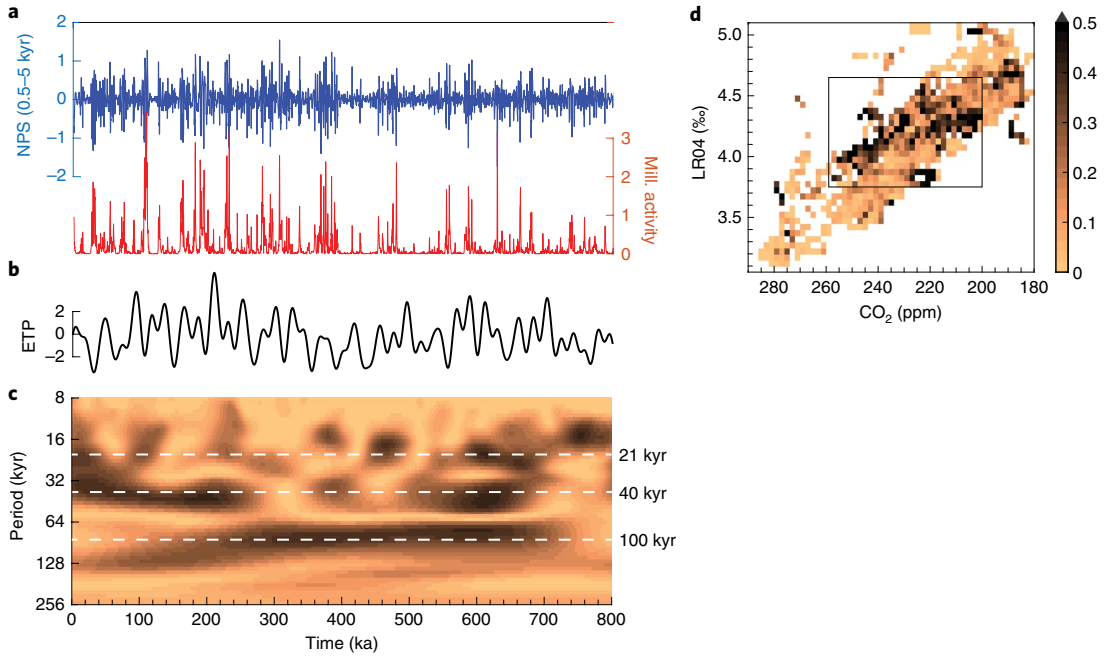

Fig. 1 | Relationship of millennial-scale climate activity with Earth's orbit and G-IG cycles in the last 800 kyr. a, The 0.5–5 kyr Taner filter (blue) results for %NPS (*Neogloboquadrina pachyderma* sinistral) in the northern North Atlantic[50], with its amplitude calculated using the Hilbert transform (red; Methods), as a measure of the millenial-scale activity. **b**, The eccentricity–tilt–precession (ETP) index (defined as a sum of three normalized orbital parameters)[27]. **c**, Wavelet coherence analysis between the millennial-scale activity (red curve in **a**) and ETP index (Methods). **d**, Millennial-scale activity in the G-IG phase space with respect to atmospheric CO_2 (ref. [37]) and the benthic $\delta^{18}O$ stack[2] over the last 800 kyr (cf. red curve in **a**). Colour represents the mean amplitude of the millennial-scale activity in a 0.05‰ (benthic $\delta^{18}O$ value) and 2 ppm (atmospheric CO_2 value) grid. Grids that include only one data point are ignored. It appears that periods of high millennial-scale activities mainly occurred under intermediate glacial conditions (rectangle in **d**). All records are anchored to the AICC2012 age model and evenly re-interpolated to 0.2-kyr resolution for the analysis (Methods).

Spontaneous AMOC oscillation

We first conducted a transient experiment (TRN40ka) with gradual changes in orbital settings from 40 ka to 32 ka (ref. [27]), based on an equilibrium baseline experiment (E40ka_CTL) in which the full boundary conditions of 40 ka were imposed for 5,000 years (Methods, Extended Data Fig. 1 and Extended Data Table 1). Following a monostable strong AMOC mode before 37 ka, the AMOC starts to fluctuate abruptly into and out of a weak AMOC phase in TRN40ka with a periodicity of ~1,200 years (Fig. 2a–c and Extended Data Fig. 2a–e), notably resembling DOs 5–7[28]. The simulated climate changes from weak to strong AMOC phases—for example, warming/cooling in the North/South Atlantic and a northward shift of the Intertropical Convergence Zone—are also in general agreement with the observed features of DOs during MIS3 (Extended Data Fig. 3a,b and Extended Data Tables 2 and 3). Therefore, the orbitally induced AMOC changes in our model provide a reasonable representation of MCV under intermediate glacial conditions.

To further test whether MCV might be a result of an unforced AMOC oscillation under constant orbital settings, we performed an equilibrium experiment (E40ka_34kaOrb) spanning ~5,500 years by changing the orbital parameters of E40ka_CTL from 40 ka to 34 ka. Although the applied orbital change is instantaneous (unlike the actual sinusoidal change), the long-term constant forcing enables us to unequivocally evaluate equilibrated climate responses and hence AMOC stability characteristics with respect to orbital change, a principle adopted in previous studies[10,12,19]. Note that 34 ka is a period corresponding to the successive DOs 5–7, during which the internal climate background (that is, ice volume[26] and atmospheric CO_2 level[25]) is relatively constant and similar to that during the 40 ka period. This lends credibility to the idea that these DOs might be a result of the existence of an AMOC oscillatory state. It appears that the AMOC shifts from a monostable strong mode in E40ka_CTL (Extended Data Fig. 1) to a stable oscillatory mode in E40ka_34kaOrb (Fig. 2d and Extended Data Fig. 2f–j). The characteristics of simulated AMOC oscillatory changes and associated global climate responses are similar to those in TRN40ka (Fig. 2c,d and Extended Data Fig. 3c,d), which is also consistent with the reconstructed features of the DOs. These confirm the existence of a supercritical Hopf bifurcation[29] associated with an orbitally controlled stable regime that has poised the AMOC for self-oscillation, accounting for the occurrences of MCV.

Governing dynamics

Earth's orbit consists of three parameters (eccentricity, precession and obliquity), which exert different effects on the temporospatial distribution of insolation across the Earth[27]. To identify their individual roles in relation to AMOC stability, we performed two further equilibrium runs in which either eccentricity-modulated precession or obliquity at 34 ka was imposed in E40ka_CTL (Fig. 3 and Extended Data Fig. 4). Both experiments were characterized by unforced AMOC oscillations, indicating that either an enhanced boreal seasonality due to a decrease in precession (E40ka_34kaEP) or an increased latitudinal insolation gradient associated with a lowered obliquity (E40ka_34kaObl) can generate a glacial climate background state under which the AMOC oscillates spontaneously.

In the scenario with enhanced boreal seasonality (E40ka_34kaEP), warmer boreal summers prompt sea-ice reduction and hence increase the open-water area in the subpolar North Atlantic (Extended Data Fig. 5d,e,g,h), which has the potential to enhance ocean heat loss during the colder boreal winter. This tends to strengthen North Atlantic Deep Water (NADW) formation by thermally increasing the surface water mass density and

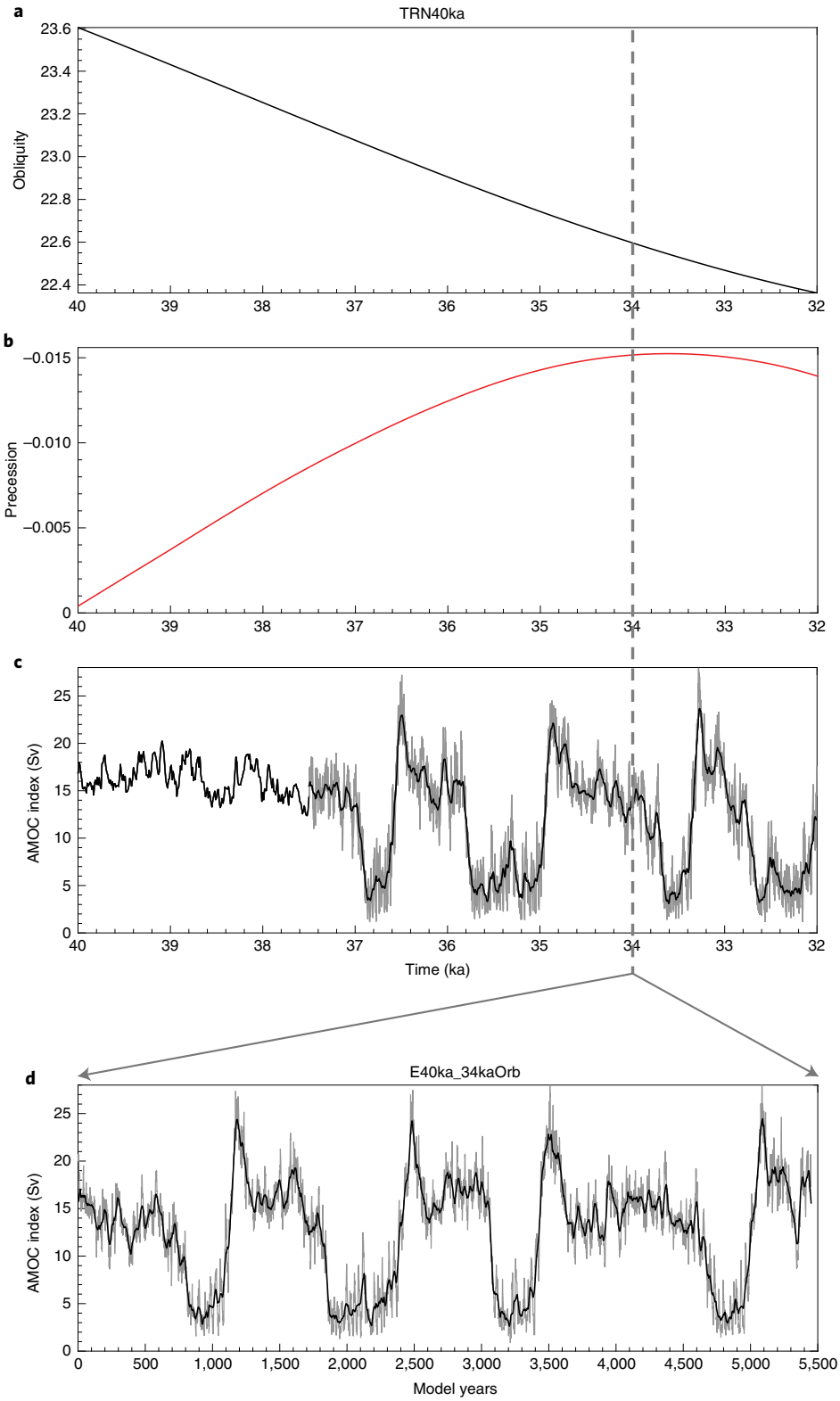

Fig. 2 | Orbitally induced AMOC oscillatory regime. a–**c**, Imposed changes in obliquity (**a**) and precession (**b**) and simulated AMOC index (**c**) in experiment TRN40ka. Note that the initial part (40–37.5 ka) of TRN40ka is accelerated by a factor of 10 (that is, 2,500 calendar years are represented by 250 model years; Methods). **d**, AMOC index in experiment E40ka_34kaOrb, representing the AMOC response to constant orbital settings of 34 ka under intermediate glacial conditions. Grey lines in **c** (at 37.5–32 ka) and **d** represent original AMOC indices from the experiments, whereas the corresponding black lines indicate 30-year running mean of the original data.

hence reducing the vertical density stratification. However, mean annual net precipitation increases synchronously over the tropical North Atlantic, effectively reducing sea-surface salinity (Fig. 3c and Extended Data Fig. 5f,i). The intensity of the western Atlantic summer warm pool has been proposed to play an important role in Atlantic-to-Pacific atmospheric moisture export by modulating

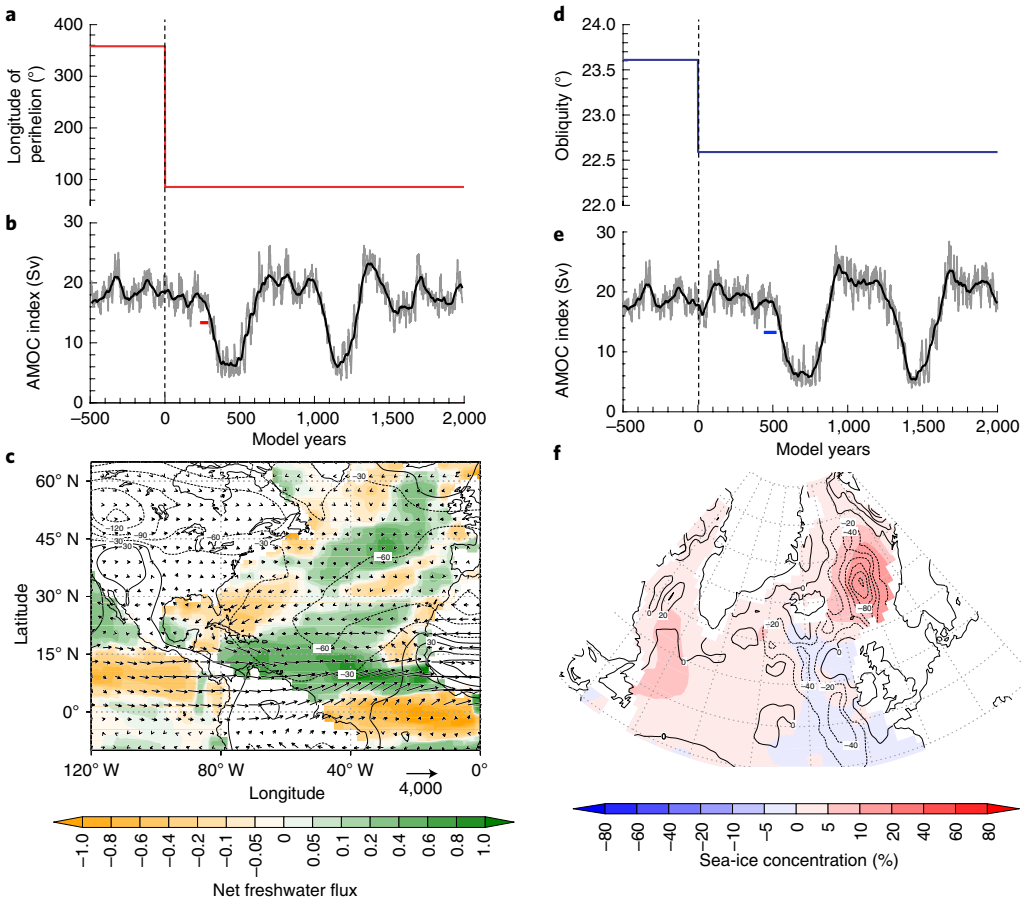

Fig. 3 | Triggering dynamics of orbitally induced AMOC changes. a,**b**, Imposed precession changes (**a**) and simulated AMOC index (**b**) in experiment E40ka_34kaEP (only changing the eccentricity-modulated precession in E40ka_CTL). **d**,**e**, Applied obliquity changes (**d**) and simulated AMOC index (**e**) in experiment E40ka_34kaObl (only changing the obliquity in E40ka_CTL). **c**,**f**, Anomalies between the mean climatology before the onset of abrupt AMOC reduction in E40ka_34kaEP (**c**) and E40ka_34kaObl (**d**) and the mean climatology of control run E40ka_CTL, representing the climate tendency after changes in precession and obliquity, respectively. The climatology in E40ka_34kaEP and E40ka_34kaObl is represented by 40- and 100-year averages of the period indicated by the red and blue bold line in **b** and **e**, respectively. Grey/black lines in **b** and **e** represent original/30-year running mean AMOC indices. Shading in **c** shows total net freshwater flux (units, mm per day), vectors (arrows) show the vertical integrated moisture transport (units, $kg\,m^{-1}\,s^{-1}$) and contours (and attached values) show sea-level pressure (units, Pa). The shading in **f** shows sea-ice concentration (units, %) and contours (and attached values) show the vertical mixed layer depth (units, m).

trade-wind strength and hence the net precipitation and sea-surface salinity in the subtropical North Atlantic[30]. In E40ka_34kaEP, the enhanced boreal summer insolation strengthens the warm pool intensity, leading to a basin-wide low-pressure anomaly[31] and hence weakened atmospheric moisture export[30] (Fig. 3c). This chain of processes was further confirmed by our sensitivity experiments in an atmospheric general circulation model (AGCM)—that is, tropical North Atlantic warming alone can reproduce a similar climate response, as illustrated in Fig. 3c (Extended Data Fig. 6). Thereafter, northward transport of these freshened tropical water masses tends to decrease the surface water density in the key convection sites of the North Atlantic, enhancing the vertical density stratification and eventually reducing NADW formation. As an equilibrated response to the increased summer insolation, the tropical freshening effect finally surpasses the subpolar warming effect, leading to a transitioning of AMOC into its weak phase (Fig. 3a–c and Extended Data Fig. 4a–e).

In E40ka_34kaObl, the lowered obliquity causes mean warming over the low latitudes but cooling over the high latitudes (that is, the scenario with enhanced latitudinal insolation gradient). The former increases the sea-surface salinity in the tropical North Atlantic by enhancing atmospheric moisture export from the western tropical North Atlantic to the eastern equatorial Pacific as a consequence of differential heating responses between them[12] (Extended Data Fig. 5a,c). This tropical hydroclimate response tends to promote formation of the NADW by supplying saltier tropical water masses to the convection sites. However, high-latitude cooling at times of low obliquity decreases the sea-surface temperature and expands sea-ice cover in the subpolar North Atlantic, reducing the open-water area where deep convection occurs and hence simultaneously decreasing the strength of the AMOC (Extended Data Fig. 5b). Under intermediate glacial conditions, sea-ice cover in the subpolar North Atlantic is close to a threshold that governs the switch between its interstadial and stadial states[10] (Extended Data Fig. 1b–e). As an equilibrated response to the lowered obliquity, the high-latitude cooling effect finally surpasses the low-latitude salinification effect, thereby leading to AMOC reduction (Fig. 3d–f).

Once a transition into the weak AMOC phase is stimulated by orbital changes (that is, TRN40ka), the contemporary constant orbital settings allow the continuation of unforced AMOC self-oscillations (that is, E40ka_34kaOrb). As the AMOC is in its weak phase, gradual subsurface warming of the subpolar ocean and increasing northward salinity transport in the North Atlantic work together to return AMOC to its strong phase. A gradual cooling in

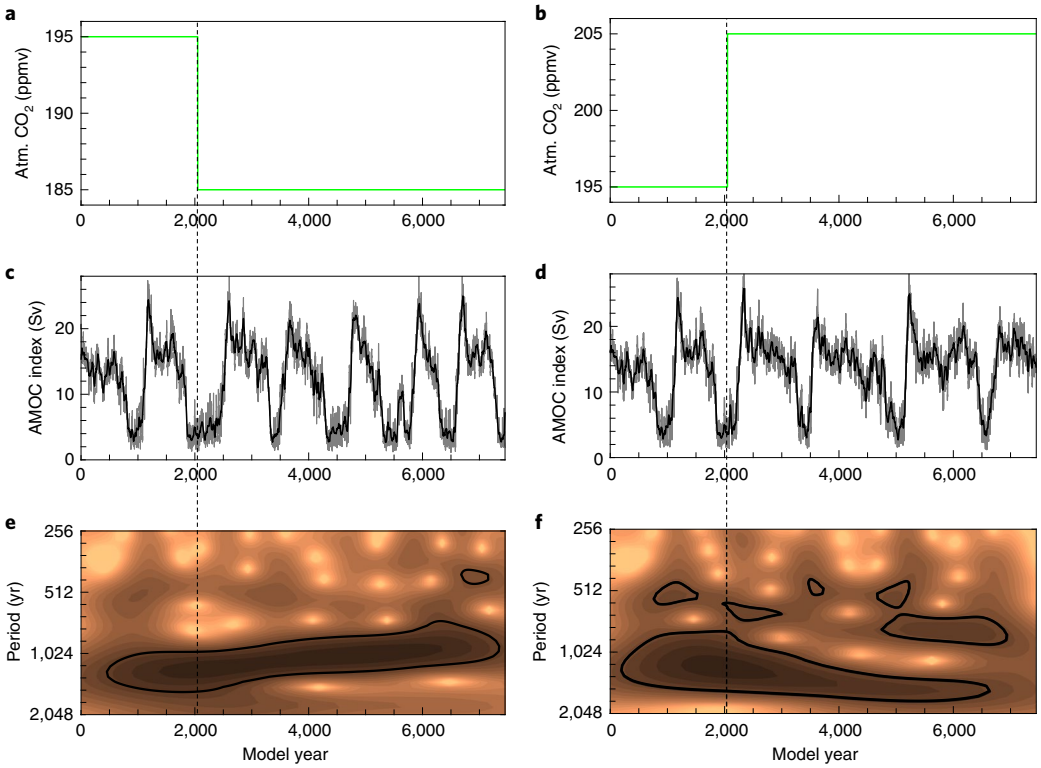

Fig. 4 | Responses of the AMOC oscillatory regime to millennial-scale CO_2 changes. a,**b**, The imposed CO_2 changes (units of parts per million volume, ppmv): a decrease in CO_2 (**a**) and an increase in CO_2 (**b**). **c**,**d**, Simulated AMOC indices corresponding to **a** and **b**, respectively. **e**,**f**, Wavelet analysis of the AMOC indices in the decreasing (**e**) and increasing (**f**) CO_2 experiments. Both CO_2 sensitivity runs are initialized from the 2,050th model year of E40ka_34kaOrb, as indicated by the vertical dashed lines. The 2,051st to 7,500th model years to the right-hand side of the dashed line correspond to the CO_2 equilibrium runs; to the left is for E40ka_34kaOrb. As the CO_2 level is decreased (increased) by 10 ppm, the dominant periodicity of AMOC oscillations (~1,200 years) is shortened (prolonged) to ~1,000 (~1,500) years after 5,000 model years, as shown in **e** (**f**).

the North Atlantic convection sites and a decrease in the northward transport of salt water cause AMOC weakening, up to a point at which the AMOC reduces abruptly and the weak phase returns (Extended Data Figs. 2 and 4). Furthermore, abrupt transitions into and out of the weak phases can be attributed to the atmosphere–ocean–sea ice positive feedback in the North Atlantic convection sites[10,32]. The unforced AMOC self-oscillation is thus a consequence of internal climate feedbacks between the low-latitude hydroclimate and the high-latitude atmosphere–ocean–sea ice system, similar to the mechanisms described for thermohaline oscillations[33–35]. Beyond this, our results show that changes in orbital parameters can modulate the North Atlantic thermohaline balance by exerting contrasting effects on NADW formation over the low versus high latitudes, generating an intrinsically oscillatory state accounting for MCV under intermediate glacial conditions.

Roles of internal climate backgrounds

Previous studies have suggested that the interplay between changes in atmospheric CO_2 and ice volume can control the sensitivity of AMOC to applied perturbations[9,10,12,19], giving rise to intermediate glacial conditions that are characterized by high MCV activity (that is, the indirect control of MCV by Earth's orbit; Fig. 1d). Indeed, no AMOC mode changes are induced in our experiments under peak glacial and interglacial conditions, even under the most extreme changes in orbital configurations (Extended Data Fig. 7 and Methods). This corroborates the dominant effects on AMOC stability of ice volume under glacial maximum conditions and of atmospheric CO_2 during peak interglacial periods during these times[10,12]. By contrast, during intermediate glacial periods, millennial-scale variations in atmospheric CO_2 of ~20 ppm (refs. [36,37]) and ice volume of ~18 m equivalent sea level (m.e.s.l.)[38] are potentially enough to alter the sensitivity of the AMOC to orbital changes. To test this hypothesis, we performed two sets of equilibrium sensitivity experiments incorporating changes in either atmospheric CO_2 (Fig. 4) or ice volume (Fig. 5) based on experiment E40ka_34kaOrb, which is characterized by an oscillatory AMOC state (Extended Data Table 1 and Methods).

In the two CO_2 sensitivity experiments in which atmospheric CO_2 level is either increased or decreased by 10 ppm, spontaneous AMOC oscillations are maintained (Fig. 4). Importantly, it appears that decreasing atmospheric CO_2 is capable of reducing the interstadial duration, thereby shortening the oscillation period (Fig. 4e,f), a concept that is consistent with ice-core records[7] (Methods). Given that AMOC changes and associated global responses can alter atmospheric CO_2 levels[22,39], this suggests that millennial-scale CO_2 changes can serve as an internal climate agent accounting for the observed changes in the timing characteristics of MCV during glacial periods.

By contrast, the AMOC is shifted to a stable weak mode in the ice-sheet sensitivity experiment in which Northern Hemisphere ice sheets are replaced by those at 50 ka, which corresponds to them being ~12 m.e.s.l. lower than those at 40 ka (phase A, Fig. 5). Further increasing the obliquity and precession (directionally opposite to the orbital changes from 40 to 34 ka) can cause a return to a stable oscillatory mode of AMOC (that is, phase A to B, Fig. 5), in which oscillating characteristics are further determined by the magnitudes of these orbital changes (that is, phase B versus C, Fig. 5 and Methods). These results suggest that decreasing Northern Hemisphere ice sheets can lead to a shift of the oscillatory regime towards higher values of obliquity and precession due to changes

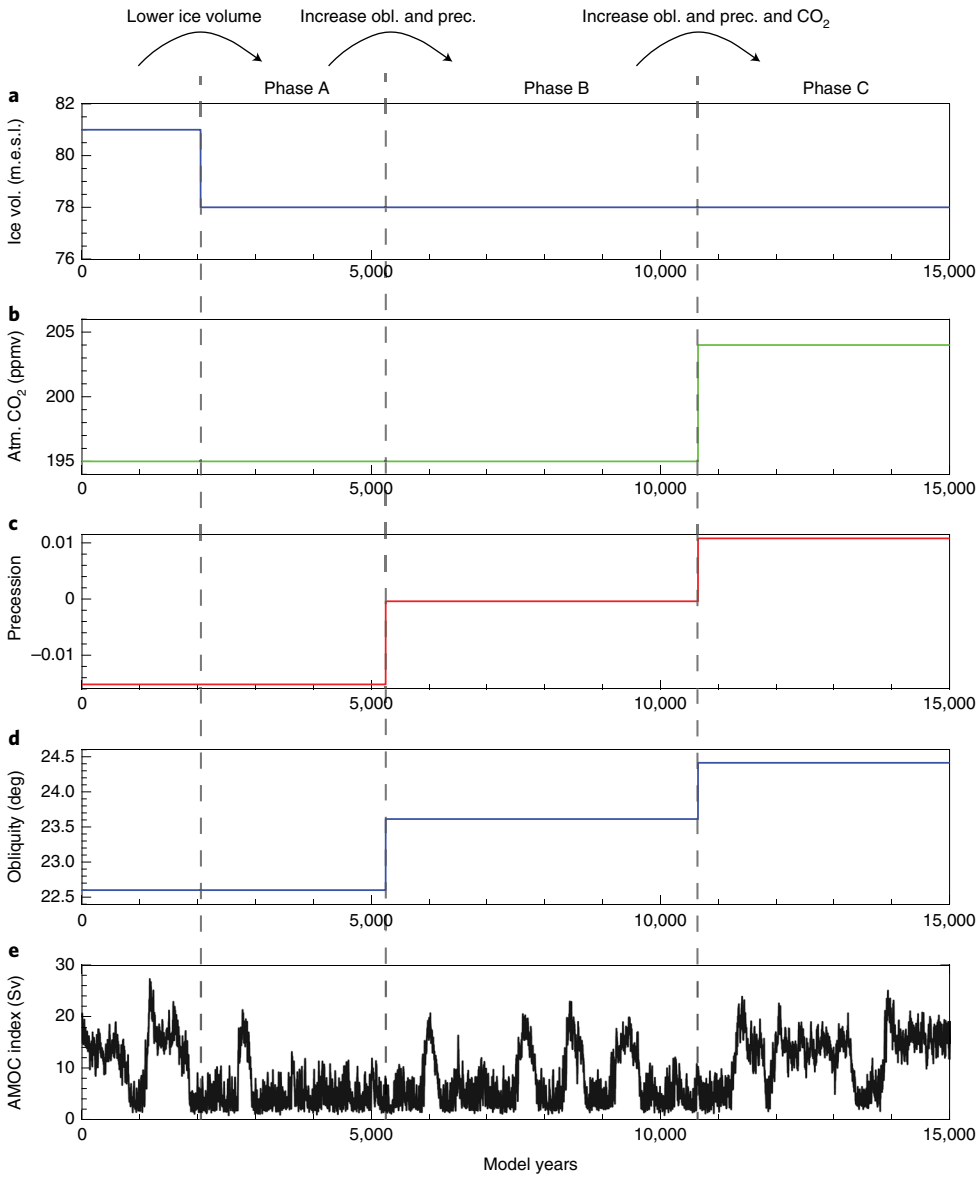

Fig. 5 | Response of the AMOC oscillatory regime to varying intermediate glacial conditions. a–d, Imposed changes in Northern Hemisphere ice sheets (**a**), atmospheric CO_2 level (**b**), precession parameter (**c**) and obliquity (**d**). **e**, Simulated AMOC index derived in turn from E40ka_34kaOrb, E40ka_34kaOrb_50kaICE (phase A), E40ka_50kaICE (phase B) and E50ka (phase C), which represent stepwise changes in boundary conditions. Note that each experiment is initialized from the quasi-equilibrium ocean state of the previous experiment, consistent with the principle to investigate AMOC hysteresis/stability behaviour (Extended Data Table 1).

in wind stress promoting sea-ice expansion and cooling across the northern North Atlantic[10].

Overall, these results suggest that climate backgrounds associated with Northern Hemisphere ice-sheet configuration and atmospheric CO_2 level determine the sensitivity of the AMOC to orbitally induced insolation changes and hence the window of the AMOC oscillatory regime in the phase space of Earth's orbital cycles (Fig. 6). Accordingly, although MCV contains evident obliquity and precessional periodicities[15–18], its amplitude does not always follow the magnitude of the associated insolation changes[40].

Oscillatory climate regime in a glacial cycle

In contrast to previous studies[20,21], the model used here, with its more advanced climate physics, enables us to elaborate on the comprehensive dynamics of the AMOC oscillatory regime associated with changes in Earth's orbit (that is, precession and obliquity) during intermediate glacial periods (that is, the direct control of MCV and abrupt climate shifts by Earth's orbit). As a result of changes in either eccentricity-modulated precession or obliquity, climate variations over the tropical and subpolar North Atlantic exert contrasting effects on the strength of the AMOC, thereby resulting in a climate background state under which unforced AMOC oscillations can occur. In particular, the subpolar thermal effect (associated with obliquity-controlled mean annual insolation) and the tropical salt effect (associated with precession-controlled summer insolation) represent the crucial triggering mechanisms of AMOC changes in response to slow variations in Earth's orbit.

Based on the simulations in this study, we synthesized a conceptual framework to describe the stable AMOC oscillatory regime in the phase space of Earth's obliquity and eccentricity-modulated precession under different internal climate backgrounds spanning G-IG cycles (Fig. 6)—that is, a framework representing the dual

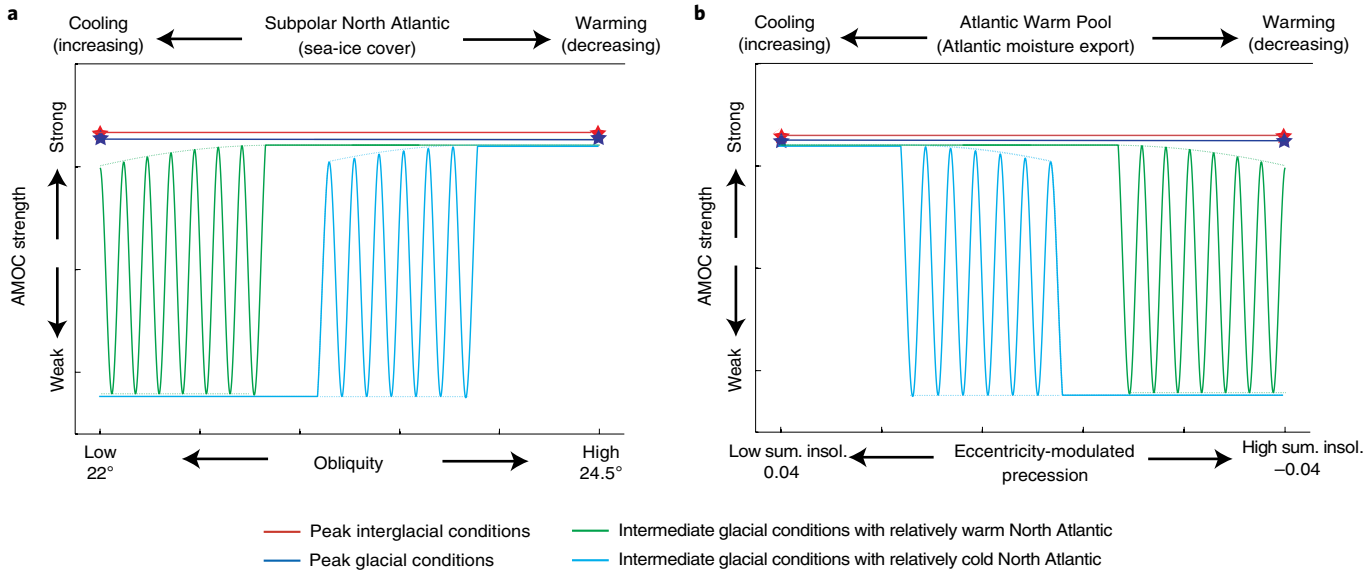

Fig. 6 | Conceptual framework for the AMOC oscillatory regime in the phase space of Earth's orbit under different climate backgrounds. a,**b**, Obliquity-modulated (**a**) and eccentricity-modulated (**b**) precession-controlled AMOC oscillatory regime under different climate backgrounds, as represented by the colour scheme. The upper *x* axis in each panel represents the governing dynamics of changes in the strength of the AMOC, associated with changes in the corresponding orbital parameters as shown in the lower *x* axis. Climate background conditions are controlled by changes in ice volume and atmospheric greenhouse gases[10,12]. Stars are indicative of orbital sensitivity runs under peak glacial (blue) and interglacial (red) conditions when orbital changes alone cannot directly give rise to AMOC mode transitions (Extended Data Fig. 7). The green and light blue lines represent scenarios under intermediate glacial conditions with a relatively warm and cold North Atlantic, respectively (in this case, the difference between warm and cold North Atlantic conditions reflects changes in ice-sheet size, but we hypothesize that CO_2 has an equivalent effect for changes in CO_2 larger than we impose in this study). In other words, the warm (cold) North Atlantic conditions correspond to scenarios with high (low) intermediate ice sheets that lead to a low (high) sensitivity of the AMOC to forcing changes[10].

controls of astronomical forcing on MCV. In particular, this shows that the oscillatory regime is a function not only of Earth's orbit under intermediate glacial conditions (Figs. 2 and 3), but also of global ice volume and (probably) atmospheric CO_2 (Fig. 5 and Extended Data Fig. 7). Note that this regime exists only under intermediate glacial conditions given the overriding influence of glacial maximum ice sheets and peak interglacial CO_2 on AMOC (mono) stability[10,12]. A recent model study[41] proposed that, under peak interglacial conditions, insolation changes alone can trigger abrupt AMOC weakening. However, the typical magnitude of AMOC weakening in their study (~5 Sv) is notably less than the AMOC changes reported here (~20 Sv). Additionally, the cooling events in their proxy records are of variable intensity and the relatively strong cooling events (for example, associated with MIS17c[41]) appear to consistently occur under intermediate glacial conditions, as defined by benthic $\delta^{18}O$ and atmospheric CO_2 in this study (Fig. 1d). Their findings[41] therefore support our contention that background climate plays a key role in the magnitude of MCV.

An evident advantage of this framework in explaining the occurrences of MCV is the independence from additional perturbations (for example, freshwater input), the origins of which are too uncertain to pin down as triggers of AMOC changes[42,43] (in contrast, changes in Earth's orbit can be unequivocally calculated[27,44]). Therefore, our framework can account for a broader spectrum of MCV in global climate archives. For example, during MIS3, some DO events (for example, DOs 5–7) that occurred without evident changes in atmospheric CO_2[25] and ice volume[26] can be explained by the orbitally induced AMOC oscillatory regime. Furthermore, given the small ratio of the number of Heinrich events (massive iceberg-releasing events) to DO cycles during MIS3[45] and the triggering dynamics of Heinrich events[23,46], our framework implies that these events might be considered as a particular case of orbitally induced MCV when Laurentide marine-based ice shelves become susceptible to subsurface warming in a weak AMOC phase.

In addition, our framework suggests that abrupt climate change could be attributed to the direct role of orbital change when contemporary changes in ice volume and atmospheric CO_2 exert opposite effects on the strength of the AMOC[10,12].

Overall, our framework represents the dual controls by changes in Earth's orbit—direct and indirect—on climate variability at millennial timescales. The former—our finding in this study—complements the classic Milankovitch theory[44] used to explain the latter, providing a coherent theoretical framework for understanding the origins of MCV and its activity across time. In particular, over the last 800 kyr, astronomical forcing can directly account for occurrences of MCV when the climate background, driven by Milankovitch cycles, is in an intermediate state as defined by benthic $\delta^{18}O$ and atmospheric CO_2 (Fig. 1d). Our results imply that MCV may also have been a direct consequence of astronomical forcing during the Early and Mid-Pleistocene when glacial cycles were characterized by different intensities and periodicities from those during the Late Pleistocene[47,48]. This is highlighted by a new 1,500-kyr-long MCV stack that consists of four centennial-scale proxies from the mid-latitude Northern Hemisphere[49]. In the real world, internal climate components (for example, ice volume, atmospheric CO_2 and ocean currents) are closely coupled[22–24] when responding to orbital changes[1]. To assess this improved Milankovitch theory in the future, Earth system models with interactive ice-sheet and carbon-cycle feedbacks will be required to explore the full dynamics associated with co-evolution of millennial- and orbital-scale climate variability during the Pleistocene.

Online content

Any methods, additional references, Nature Research reporting summaries, source data, extended data, supplementary information, acknowledgements, peer review information; details of author contributions and competing interests; and statements of data and code availability are available at https://doi.org/10.1038/s41561-021-00846-6.

Received: 29 January 2020; Accepted: 22 September 2021;
Published online: 1 November 2021

References

1. Hays, J. D., Imbrie, J. & Shackleton, N. J. J. Variations in the Earth' s orbit: pacemaker of the ice ages. *Science* **194**, 1121–1132 (1976).
2. Lisiecki, L. E. & Raymo, M. E. A Pliocene–Pleistocene stack of 57 globally distributed benthic $\delta^{18}O$ records. *Paleoceanography* **20**, 1–17 (2005).
3. Raymo, M. E., Ganley, K., Carter, S., Oppo, D. W. & McManus, J. Millennial-scale climate instability during the early Pleistocene epoch. *Nature* **392**, 699–702 (1998).
4. McManus, J. F., Oppo, D. W. & Cullen, J. L. A 0.5-million-year record of millennial-scale climate variability in the North Atlantic. *Science* **283**, 971–975 (1999).
5. Jouzel, J. et al. Orbital and millennial Antarctic climate variability over the past 800,000 years. *Science* **317**, 793–796 (2007).
6. Hodell, D. A. & Channell, J. E. T. Mode transitions in Northern Hemisphere Glaciation: co-evolution of millennial and orbital variability in Quaternary climate. *Clim. Past* **12**, 1805–1828 (2016).
7. Brook, E. J. & Buizert, C. Antarctic and global climate history viewed from ice cores. *Nature* **558**, 200–208 (2018).
8. Dansgaard, W. et al. Evidence for general instability of past climate from a 250-kyr ice-core record. *Nature* **364**, 218–220 (1993).
9. Ganopolski, A. & Rahmstorf, S. Rapid changes of glacial climate simulated in a coupled climate model. *Nature* **409**, 153–158 (2001).
10. Zhang, X., Lohmann, G., Knorr, G. & Purcell, C. Abrupt glacial climate shifts controlled by ice sheet changes. *Nature* **512**, 290–294 (2014).
11. Peltier, W. R. & Vettoretti, G. Dansgaard–Oeschger oscillations predicted in a comprehensive model of glacial climate: a 'kicked' salt oscillator in the Atlantic. *Geophys. Res. Lett.* **41**, 7306–7313 (2014).
12. Zhang, X., Knorr, G., Lohmann, G. & Barker, S. Abrupt North Atlantic circulation changes in response to gradual CO_2 forcing in a glacial climate state. *Nat. Geosci.* **10**, 518–523 (2017).
13. Lynch-Stieglitz, J. The Atlantic meridional overturning circulation and abrupt climate change. *Ann. Rev. Mar. Sci.* **9**, 83–104 (2017).
14. Barker, S. et al. 800,000 years of abrupt climate variability. *Science* **334**, 347–351 (2011).
15. Siddall, M., Rohling, E. J., Blunier, T. & Spahni, R. Patterns of millennial variability over the last 500 ka. *Clim. Past* **6**, 295–303 (2010).
16. Cheng, H. et al. The Asian monsoon over the past 640,000 years and ice age terminations. *Nature* **534**, 640–646 (2016).
17. McIntyre, A. & Molfinot, B. Forcing of Atlantic equatorial and subpolar millennial cycles by precession. *Science* **274**, 1867–1870 (1996).
18. Thirumalai, K., Clemens, S. C. & Partin, J. W. Methane, monsoons and modulation of millennial-scale climate. *Geophys. Res. Lett.* **47**, e2020GL087613 (2020).
19. Zhang, X., Prange, M., Merkel, U. & Schulz, M. Instability of the Atlantic overturning circulation during Marine Isotope Stage 3. *Geophys. Res. Lett.* **41**, 4285–4293 (2014).
20. Rial, J. A. & Yang, M. Is the frequency of abrupt climate change modulated by the orbital insolation? *Geophys. Monogr. Ser.* **173**, 167–174 (2007).
21. Mitsui, T. & Crucifix, M. Influence of external forcings on abrupt millennial-scale climate changes: a statistical modelling study. *Clim. Dyn.* **48**, 2729–2749 (2017).
22. Schmittner, A. & Galbraith, E. D. Glacial greenhouse-gas fluctuations controlled by ocean circulation changes. *Nature* **456**, 373–376 (2008).
23. Marcott, S. A. et al. Ice-shelf collapse from subsurface warming as a trigger for Heinrich events. *Proc. Natl Acad. Sci. USA* **108**, 13415–13419 (2011).
24. Markle, B. R. et al. Global atmospheric teleconnections during Dansgaard–Oeschger events. *Nat. Geosci.* **10**, 36–40 (2017).
25. Ahn, J. & Brook, E. J. Siple Dome ice reveals two modes of millennial CO_2 change during the last ice age. *Nat. Commun.* **5**, 3723 (2014).
26. Grant, K. M. et al. Rapid coupling between ice volume and polar temperature over the past 150,000 years. *Nature* **491**, 744–747 (2012).
27. Laskar, J. et al. A long term numerical solution for the insolation quantities of the Earth. *Astron. Astrophys.* **428**, 261–285 (2004).
28. Grootes, P. M. & Stuiver, M. Oxygen 18/16 variability in Greenland snow and ice with 10^{-3} to 10^5-year time resolution. *J. Geophys. Res. Oceans* **102**, 26455–26470 (1997).
29. Marsden, S. E., & McCracken, M. *The Hopf Bifurcation and Its Applications.* (Springer-Verlag, New York. 976).
30. Wang, C., Zhang, L. & Lee, S.-K. Response of freshwater flux and sea surface salinity to variability of the Atlantic warm pool. *J. Clim.* **26**, 1249–1267 (2013).
31. Gill, A. E. Some simple solutions for heat-induced tropical circulation. *Q. J. R. Meteorol. Soc.* **106**, 447–462 (1980).
32. Li, C. & Born, A. Coupled atmosphere-ice-ocean dynamics in Dansgaard-Oeschger events. *Q. Sci. Rev* **203**, 1–20 (2019).
33. Winton, M. in *Ice in the Climate System* (ed. Peltier, W. R.) 417–432 (Springer, 1993).
34. Brown, N. & Galbraith, E. D. Hosed vs. unhosed: interruptions of the Atlantic Meridional Overturning Circulation in a global coupled model, with and without freshwater forcing. *Clim. Past* **12**, 1663–1679 (2016).
35. Broecker, W. S., Bond, G., Klas, M., Bonani, G. & Wolfli, W. A salt oscillator in the Glacial Atlantic? 1. The concept. *Paleoceanography* **5**, 469–477 (1990).
36. Ahn, J. & Brook, E. J. Atmospheric CO_2 and climate on millennial time scales during the last glacial period. *Science* **83**, 83–85 (2008).
37. Bereiter, B. et al. Revision of the EPICA Dome C CO_2 record from 800 to 600 kyr before present. *Geophys. Res. Lett.* **42**, 542–549 (2015).
38. Siddall, M., Rohling, E. J., Thompson, W. G. & Waelbroeck, C. Marine Isotope Stage 3 sea level fluctuations: data synthesis and new outlook. *Rev. Geophys.* **46**, RG000226 (2008).
39. Gottschalk, J. et al. Mechanisms of millennial-scale atmospheric CO_2 change in numerical model simulations. *Q. Sci. Rev.* **220**, 30–74 (2019).
40. Billups, K. & Scheinwald, A. Origin of millennial-scale climate signals in the subtropical North Atlantic. *Paleoceanography* **29**, 612–627 (2014).
41. Yin, Q. Z., Wu, Z. P., Berger, A., Goosse, H. & Hodell, D. Insolation triggered abrupt weakening of Atlantic circulation at the end of interglacials. *Science* **373**, 1035–1040 (2021).
42. Dokken, T. M., Nisancioglu, K. H., Li, C., Battisti, D. S. & Kissel, C. Dansgaard-Oeschger cycles: interactions between ocean and sea ice intrinsic to the Nordic Seas. *Paleoceanography* **28**, 491–502 (2013).
43. Barker, S. et al. Icebergs not the trigger for North Atlantic cold events. *Nature* **520**, 333–336 (2015).
44. Milanković, M. *Kanon der Erdbestrahlung und seine Anwendung auf das Eiszeitenproblem*, Royal Serbien Sciences, Special Publications 132, Section of Mathematical and Natural Sciences 133 (Royal Serbian Academy, 1941).
45. Heinrich, H. Origin and consequences of cyclic ice rafting in the Northeast Atlantic Ocean during the past 130,000 years. *Quat. Res.* **29**, 142–152 (1988).
46. Bassis, J. N., Petersen, S. V. & Mac Cathles, L. Heinrich events triggered by ocean forcing and modulated by isostatic adjustment. *Nature* **542**, 332–334 (2017).
47. Shackleton, N. J. & Opdyke, N. D. Oxygen-isotope and paleomagnetic stratigraphy of pacific core V28-239 late Pliocene to latest Pleistocene. *Geological Society of America Memoir.* **145**, 449–464 (1976).
48. Pisias, N. G. & Moore, T. C. The evolution of Pleistocene climate: a time series approach. *Earth Planet. Sci. Lett.* **52**, 450–458 (1981).
49. Sun, Y. et al. Persistent orbital influence on millennial climate variability through the Pleistocene. *Nat. Geosci.* https://doi.org/10.1038/s41561-021-00794-1 (2021).
50. Barker, S. et al. Early interglacial legacy of deglacial climate instability. *Paleoceanogr. Paleoclimatol.* **34**, 1455–1475 (2019).

Publisher's note Springer Nature remains neutral with regard to jurisdictional claims in published maps and institutional affiliations.

© The Author(s), under exclusive licence to Springer Nature Limited 2021

Methods

Time-series analysis. Bandpass filtering was performed on evenly resampled (0.2 kyr) time series using a Taner filter (roll-off rate = 1×10^{12}) with the MATLAB function presented by L. A. Hinnov (http://mason.gmu.edu/~lhinnov/cyclostratigraphytools.html). Hilbert transforms of the bandpass-filtered series were also implemented using L. A. Hinnov's MATLAB function. Wavelet analyses were produced using the MATLAB function presented by Grinsted et al.[51], implemented on evenly resampled (0.2 kyr) time series.

Model description. We used a comprehensive fully coupled atmosphere–ocean general circulation model (AOGCM), COSMOS (ECHAM5-JSBACH-MPI-OM). The atmospheric model ECHAM5[52], complemented by the land surface component JSBACH[53], was used at T31 resolution (~3.75°), with 19 vertical layers. The ocean model MPI-OM[54], including sea-ice dynamics formulated using viscous-plastic rheology[55], has a resolution of GR30 (3° × 1.8°) in the horizontal, with 40 uneven vertical layers. This climate model has already been used to investigate a range of palaeoclimate phenomena[56–60], especially millennial-scale abrupt glacial climate changes[10,12]. This indicates that it is capable of capturing the nonlinear behaviour of the glacial climate system and is thus a very suitable climate model for this study.

Experimental details. All experiments performed in this study are listed in Extended Data Table 1. A detailed introduction of each type of experiment and their rationality are presented as follows.

MIS3 baseline experiment. We first conducted an equilibrated control simulation (E40ka_CTL) by imposing the fixed boundary conditions of 40 ka. Specifically, during 40 ka, the three orbital parameters (eccentricity, precession of the equinoxes (the angle between the Earth's position during the Northern Hemisphere vernal equinox and the orbit perihelion) and obliquity) are 0.013146, 358.17° and 23.61°, respectively[27], and the greenhouse gases CO_2, CH_4 and N_2O are at 195 ppm, 413 ppb and 231 ppb, respectively[25,61]. The ice-sheet configuration is a combination of ice-sheet reconstructions from ICE-5G[62] and Paleoclimate Model Inter-comparison Project 3 (PMIP3). In other words, we first calculated the topography anomaly between 40 ka and the Last Glacial Maximum (LGM) in ICE-5G and then added it to the PMIP3 LGM topography[58]. Global mean sea level was ~80 m.e.s.l. lower at 40 ka than the pre-industrial level. E40ka_CTL was integrated for 5,000 years to an equilibrated state that served as a basis for the following sensitivity experiments.

Hosing experiment. The AMOC in E40ka_CTL is in a strong mode. To test whether it is stable we performed a classic North Atlantic hosing experiment (E40ka_fwf) based on E40ka_CTL (Extended Data Table 1). In E40ka_fwf, freshwater flux of 0.15 Sv (1 Sv = 10^6 m^3 s^{-1}) was imposed into the Ruddiman belt for 500 years to mimic Heinrich event 4 (HE4; a massive iceberg-releasing event). Once the hosing was removed at the 501st model year, the AMOC recovered abruptly from a weak to a strong mode and remained strong during the following 1,500 years (Extended Data Fig. 1a). This suggests that the AMOC is in a monostable strong mode under the 40 ka boundary conditions (that is, in E40ka_CTL). This rules out the previous assertion that freshwater perturbation (that is, a Heinrich event) might be a potential precondition for the following DOs[8,63].

Transient experiment of 40–32 ka. To test whether orbital changes alone can give rise to millennial-scale climate variability, based on E40ka_CTL we performed a transient experiment by only varying the orbital settings from 40 ka to 32 ka (TRN40ka) (Extended Data Table 1). The imposed orbital parameters were calculated based on those in ref. [27] (Fig. 2a,b). Because our focus is on DOs 5–7, we employed an acceleration factor of 10 to simulate the time interval between 40 ka and 37.5 ka (that is, 250 model years represent 2,500 calendar years) to accelerate the experiment. The TRN40ka experiment was thus integrated for 5,750 model years to represent the time interval between 40 and 32 ka.

Sensitivity experiments under intermediate glacial conditions. To evaluate equilibrium climate responses to certain constant orbital settings, three experiments, E40ka_34kaOrb, E40ka_34kaEP and E40ka_34kaObl, were performed based on E40ka_CTL (same initial ocean state as TRN40ka). In E40ka_34kaOrb, the three orbital parameters[27] were set to those at 34 ka—that is, eccentricity of 0.014996, precession of 84.84° and obliquity of 22.6°—while the other boundary conditions (for example, greenhouse gases and ice-sheet configuration) were fixed to E40ka_CTL. In E40ka_34kaObl (E40ka_34kaEP), obliquity (eccentricity-modulated precession) was set to 34 ka, and the other parameters were identical to those of E40ka_CTL. E40ka_34kaOrb was integrated for 5,500 years to explore the equilibrated responses of glacial climate to the 34 ka orbital configurations. E40ka_34kaEP and E40ka_34kaObl were integrated for 2,000 years because they are mainly used to evaluate whether changes in obliquity or precession alone can account for AMOC oscillations (Extended Data Table 1 and Extended Data Figs. 4 and 5).

In E40ka_34kaOrb, we observed unforced AMOC oscillation with a periodicity of ~1,500 years. To evaluate the role of millennial-scale variation in atmospheric CO_2 levels on the unforced oscillation, we performed two sensitivity experiments by instantly increasing (E40ka_34kaOrb_pCO2) or decreasing (E40ka_34kaOrb_nCO2) CO_2 levels by 10 ppm at the 2,050th model year of E40ka_34kaOrb and integrated both of them for 5,400 years to assess their equilibrium responses to these CO_2 changes. In both experiments, spontaneous DO-like AMOC oscillations were sustained, indicating that millennial-scale CO_2 variability (~20 ppm) cannot shift the AMOC out of the window of its oscillating regime (Fig. 4). This is probably due to the fact that atmospheric CO_2 changes from 205 to 185 ppm are equivalent to changes in radiative forcing of ~0.55 W m^{-2} (ref. [64]), which are too weak to overcome the impacts of insolation changes. Nevertheless, these changes can alter the thermohaline balance between the low- and high-latitude North Atlantic[12], affecting the timing characteristics of the oscillations. In other words, decreasing atmospheric CO_2 is capable of reducing interstadial durations, thereby shortening the oscillating periodicity (Fig. 4). During MIS3, durations of warm interstadials have a close relationship with Antarctic/Southern Ocean temperatures, which share a close correspondence with changes in atmospheric CO_2 (refs. [5,7,37]). For example, the successive DOs 5–7 have a decreasing interstadial duration along with a cooling background associated with a gradual CO_2 decline of ~15 ppm (refs. [5,7,8,25,37]). Accordingly, these results, in addition to the notion that changes in the AMOC and associated global response are thought to alter atmospheric CO_2 levels, suggest that millennial-scale CO_2 changes may serve as an internal climate agent modulating timing characteristics of millennial-scale climate variability during glacial periods.

To evaluate the role of millennial-scale changes in global mean sea level during MIS3, we instantly altered the ice-sheet configuration of 40 ka to that of 50 ka at the 2,050th model year of E40ka_34kaOrb and integrated it for 3,200 model years (E40ka_34kaOrb_50kaICE). Note that the way of generating the 50 ka ice-sheet configuration is identical to that for 40 ka. The ice volume at 50 ka is ~12.5 m.e.s.l. lower than at 40 ka according to ICE-5G[62]. In this 3,200-year experiment, the AMOC shifts from its stable oscillating mode to a stable weak mode, indicating the important role of ice-sheet changes in altering the oscillating properties (phase A, Fig. 5). This is due to the associated changes in atmospheric circulation[7,59], which on the one hand enhances sea-ice transport from the Labrador Sea to the key convection sites and on the other hand weakens the subtropical gyre to transport warm and salty water northwards. This alters the tropical and subpolar thermohaline balances in the North Atlantic in E40ka_34kaOrb, resulting in a weak AMOC mode under a lower ice-volume configuration with the same orbital forcing to E40ka_34kaOrb.

According to the governing mechanisms of unforced AMOC oscillation, it is likely that increasing obliquity and eccentricity-modulated precession (opposite to orbital changes from 40 ka to 34 ka) can restart AMOC self-oscillations under the low ice-volume configuration (phase A, Fig. 5). We thus performed an experiment (E40ka_50kaICE) in which we instantly imposed the 40 ka orbital configurations in E40ka_34kaOrb_50kaICE (at the 5,250th model year, as shown in Fig. 5) for 5,400 model years. As expected, the AMOC oscillating mode was reinitiated (phase B, Fig. 5). Notably, these oscillations in E40ka_50kaICE are not characterized by the classic sawtooth-like variation (relatively stable stadial conditions, with occasional returns to interstadial conditions). This is attributed to the lowered Northern Hemisphere ice volume, such that impacts on the tropical and subpolar thermohaline balance in the North Atlantic remain dominant, resulting in a state in which the weak AMOC phase is relatively stable under the 40 ka orbital configurations. Changing the orbital settings further back to 50 ka—a period with higher obliquity and precession than during the 40 ka period—produces a return of the classic sawtooth-like AMOC oscillation (phase C, Fig. 5). These stepwise transient experiments (Fig. 5) corroborate the governing role of orbital changes in the unforced AMOC oscillatory regime under various intermediate ice-sheet configurations.

Sensitivity experiments under peak interglacial and glacial maximum conditions. Previous studies have proposed that changes in internal climate backgrounds can control the sensitivity of the AMOC to applied perturbations[9,10,12,19]. In particular, high atmospheric CO_2 levels during peak interglacials and high Northern Hemisphere ice sheets during glacial maxima will give rise to a very stable AMOC with a high resistance to additional internal climate perturbations. To test whether this assertion holds for insolation changes, we designed a set of orbital sensitivity experiments under the LGM or pre-industrial conditions by applying extreme orbital settings of the last two million years; that is, eccentricity-modulated precession was set to either −0.04 or 0.04 and obliquity was set to either 22° or 24.5°. This resulted in four different sensitivity experiments under each boundary conditions (Extended Data Table 1). We integrated each experiment for 1,500 years to ensure a quasi-equilibrium climate. As suggested, no AMOC mode transitions occurred in these runs (Extended Data Fig. 7), confirming the previous assertion about the dominant roles of atmospheric CO_2 and Northern Hemisphere ice-sheet height on AMOC stability.

Experiments in an AGCM. Present-day observations suggest that changes in the Atlantic warm pool intensity play an important role in mean Atlantic-to-Pacific moisture export[30]. That is, an enhanced and expanded Atlantic warm pool reduces moisture export by stimulating anomalous convergent flow and a weak trade wind in the North Atlantic[30]. This, in addition to the notion that the Atlantic warm pool mainly appears during the boreal summer[65], indicates that Earth's precession can

modulate mean hydrology cycles in the tropical North Atlantic via the impacts of summer insolation on the Atlantic warm pool intensity. To confirm this, as well as the associated dynamics at a precessional timescale, we conducted a series of sensitivity experiments in an AGCM, ECHAM5. The key goal of the AGCM experiments is to explore equilibrated climate responses to precession change and the associated dynamics under conditions without evident change in the AMOC. This can largely minimize the uncertainty caused by ocean processes adjusting to an oscillatory AMOC mode. The AMOC under LGM conditions is always in a stable strong mode, even if applying extreme summer insolation changes by shifting Earth's position from aphelion (LGM_Hobl_LSea) to perihelion (LGM_Hobl_HSea) during the boreal summer solstice, unlike the cases under the 40 ka conditions (E40ka_CTL and E40ka_34kaEP). Accordingly, we employed the results from these precessional sensitivity experiments under LGM conditions. The experimental ID with prefix 'A_' represents AGCM experiments to distinguish from experiments in a coupled climate model. Each AGCM experiment was integrated for 50 years, and the average of the last 30 years was used to represent the corresponding climatology.

To first confirm that the AGCM can capture climate responses derived from the coupled model, we conducted two experiments, A_CTL and A_ORB_SST, by applying full forcing (that is, sea surface temperature (SST), sea ice concentration (SIC) and orbital settings) from LGM_Hobl_LSea and LGM_Hobl_HSea, respectively. In line with the results from the coupled model (Extended Data Fig. 6a), the AGCM results well reproduce the key features of the climate response to an increase in boreal summer insolation (Extended Data Fig. 6b). All other AOGCM experiments were based on the settings in A_CTL, unless specified differently. To assess the contributions of terrestrial and oceanic responses to overall climate responses in A_ORB_SST, we conducted two experiments, A_ORB and A_SST, by applying either orbital settings or SST and SIC from LGM_Hobl_HSea, respectively. Note that applying the orbital settings alone only causes a terrestrial temperature change in the AGCM. As shown in Extended Data Fig. 7c,d, by only applying oceanic changes the AGCM can reproduce a similar climate response to A_ORB_SST (Extended Data Fig. 6b). Accordingly, we performed an experiment directly relevant to our hypothesis, A_TroNASST, in which we only imposed the SST changes in the subtropical North Atlantic where the Atlantic warm pool is located (Extended Data Fig. 6e). It appears that A_TroNASST can well reproduce the enhanced net precipitation by trapping more moisture in the North Atlantic, similar to A_ORB_SST and A_SST. Together with the A_ORB_EPSST experiment, in which orbital settings and SST changes were only applied in the equatorial eastern Pacific (Extended Data Fig. 7f), this substantiates that precessional changes in the Atlantic warm pool intensity play a dominant role in hydrology changes in the North Atlantic.

Data–model comparison. A model–data comparison is a valuable approach to analyse both the simulated model results and proxy-based reconstructions. During the G-IG cycles of the last 800 kyr, MIS3 is characterized with the greatest abundance of proxy records that are able to resolve MCV globally[66]. Here we compare our model results with 44 published proxy records (Extended Data Tables 2 and 3) to qualitatively assess the reliability of the simulated spontaneous AMOC oscillation (AMOC instability) for explaining MCV under intermediate glacial conditions (Extended Data Fig. 3).

As shown in Extended Data Fig. 2a,b,f,g, it is evident that the abrupt warming in the Northern Hemisphere is in concert with a rapid AMOC transition with latitudinal shifts of the main convection sites (not shown), consistent with the inferences derived from $\delta^{13}C$ and magnetic records for DO events during MIS3 (see for example refs. [67,68]). Along with an abrupt AMOC transition from its weak to its strong phase, evident changes in global precipitation and surface temperature patterns are also well recorded in a variety of global proxy datasets (Extended Data Fig. 3 and Extended Tables 2 and 3)[69–110]. In both TRN40ka and E40ka_34kaOrb, the Atlantic bipolar thermal seesaw, which is clearly documented in palaeoclimate reconstructions from the North and South Atlantic (see for example refs. [66,86,111]), is generally captured in our model simulations (Extended Data Fig. 3a,c). Our model simulates the global and regional responses of surface temperature to AMOC change very well, although it underestimates the warming magnitudes, especially over Greenland, which can be potentially attributed to an underestimation of sea-ice responses in the Nordic Sea to the AMOC change[10,112]. The Intertropical Convergence Zone shifts northward as Northern Hemisphere warming occurs, as indicated by proxy data (Extended Data Fig. 3b,d). In response to the enhanced AMOC, increased water vapour is transported further northward from the mid latitudes to high latitudes in the North Atlantic, leading to a drying phase over the subtropics (for example, mid-Florida)[93] and a wet phase over the Northeast Atlantic (for example Europe)[89]. The northern warming also strengthens the Asian summer monsoons, which are characterized by an evident increase in precipitation. In conclusion, the two AMOC phases in the AMOC oscillatory regime related to orbital changes can well capture key features of DO events (see for example refs. [66,86]), adding credibility to our proposed mechanism for explaining abrupt climate shifts during intermediate glacial conditions.

Atlantic meridional salinity transport. To diagnose the meridional salinity transport associated with AMOC (M_{ov}) across the boundary between the North Atlantic subpolar and subtropical gyre (~43° N), we use the equation widely used to evaluate freshwater import or export across the southern boundary of the Atlantic[113] but reverse its sign:

$$M_{ov} = \frac{1}{S_0}\int dz\, \bar{v}(z)\,[\langle S(z)\rangle - S_0]$$

where S_0 is the Atlantic mean salinity value, and the overbar and angle brackets denote zonal integration and zonal averaging along one latitude, respectively.

Data availability

The palaeoclimate records used in this paper are available at the following sources: ref. [2], benthic $\delta^{18}O$ stack, https://doi.pangaea.de/10.1594/PANGAEA.704257; ref. [37], CO_2 data, http://onlinelibrary.wiley.com/store/10.1002/2014GL061957/asset/supinfo/grl52461-sup-0003-supplementary.xls?v=1&s=e77ad89c3925111330671009ab40eac65e019d01; ref. [50], ODP983 NPS data, https://doi.pangaea.de/10.1594/PANGAEA.904398. The model data that supports the key findings of this study are available in National Tibetan Plateau Data Center (TPDC) at https://doi.org/10.11888/Paleoenv.tpdc.271670.

Code availability

The standard model code of the 'Community Earth System Models' (COSMOS) version COSMOS-landveg r2413 (2009) is available upon request from the 'Max Planck Institute for Meteorology' in Hamburg (https://www.mpimet.mpg.de). Post-processing of the model output and model data analysis were performed with CDO (Climate Data Operators, version 1.9.5 and 1.9.10, https://code.mpimet.mpg.de/projects/cdo).

References

51. Grinsted, A., Moore, J. C. & Jevrejeva, S. Application of the cross wavelet transform and wavelet coherence to geophysical time series. *Nonlinear Process. Geophys.* **11**, 561–566 (2004).
52. Roeckner, E. et al. *The Atmospheric General Circulation Model ECHAM5. Part 1: Model Description* (Max-Planck-Institut für Meteorologie, 2003).
53. Brovkin, V., Raddatz, T., Reick, C. H., Claussen, M. & Gayler, V. Global biogeophysical interactions between forest and climate. *Geophys. Res. Lett.* **36**, L07405 (2009).
54. Marsland, S. J., Haak, H., Jungclaus, J. H., Latif, M. & Röske, F. The Max-Planck-Institute global ocean/sea ice model with orthogonal curvilinear coordinates. *Ocean Model.* **5**, 91–127 (2003).
55. Hibler, W. III A dynamic thermodynamic sea ice model. *J. Phys. Oceanogr.* **9**, 815–846 (1979).
56. Wei, W. & Lohmann, G. Simulated Atlantic multidecadal oscillation during the Holocene. *J. Clim.* **25**, 6989–7022 (2012).
57. Gong, X., Knorr, G., Lohmann, G. & Zhang, X. Dependence of abrupt Atlantic meridional ocean circulation changes on climate background states. *Geophys. Res. Lett.* **40**, 3698–3704 (2013).
58. Zhang, X., Lohmann, G., Knorr, G. & Xu, X. Different ocean states and transient characteristics in Last Glacial Maximum simulations and implications for deglaciation. *Clim. Past* **9**, 2319–2333 (2013).
59. Knorr, G. & Lohmann, G. Climate warming during Antarctic ice sheet expansion at the Middle Miocene transition. *Nat. Geosci.* **7**, 376–381 (2014).
60. Stärz, M., Jokat, W., Knorr, G. & Lohmann, G. Threshold in North Atlantic–Arctic Ocean circulation controlled by the subsidence of the Greenland–Scotland Ridge. *Nat. Commun.* **8**, 15681 (2017).
61. Köhler, P., Nehrbass-Ahles, C., Schmitt, J., Stocker, T. F. & Fischer, H. A 156 kyr smoothed history of the atmospheric greenhouse gases CO_2, CH_4 and N_2O and their radiative forcing. *Earth Syst. Sci. Data* **9**, 363–387 (2017).
62. Peltier, W. R. Global glacial isostasy and the surface of the ice-age Earth: the ICE-5G (VM2) Model and GRACE. *Annu. Rev. Earth Planet. Sci.* **32**, 111–149 (2004).
63. Hemming, S. Heinrich events: massive Late Pleistocene detritus layers of the North Atlantic and their global climate imprint. *Rev. Geophys.* **42**, RG1005 (2004).
64. Myhre, G., Highwood, E. J., Shine, K. P. & Stordal, F. New estimates of radiative forcing due to well mixed greenhouse gases. *Geophys. Res. Lett.* **25**, 2715–2718 (1998).
65. Wang, C., Enfield, D. B., Lee, S. K. & Landsea, C. W. Influences of the Atlantic warm pool on western hemisphere summer rainfall and Atlantic hurricanes. *J. Clim.* **19**, 3011–3028 (2006).
66. Voelker, A. H. L. Global distribution of centennial-scale records for Marine Isotope Stage (MIS) 3: a database. *Quat. Sci. Rev.* **21**, 1185–1212 (2002).
67. Kissel, C., Laj, C., Labeyrie, L. & Dokken, T. Rapid climatic variations during marine isotopic stage 3: magnetic analysis of sediments from Nordic Seas and North Atlantic. *Earth Planet. Sci. Lett.* **171**, 489–502 (1999).
68. Elliot, M., Labeyrie, L. & Duplessy, J. Changes in North Atlantic deep-water formation associated with the Dansgaard-Oeschger temperature oscillations (60–10 ka). *Quat. Sci. Rev.* **21**, 1153–1165 (2002).

69. Grootes, P. M., Stulver, M., White, J. W. C., Johnsen, S. & Jouzel, J. Comparison of oxygen isotope records from the GISP2 and GRIP Greenland ice cores. *Nature* **366**, 552–554 (1993).
70. Huber, C. et al. Isotope calibrated Greenland temperature record over Marine Isotope Stage 3 and its relation to CH_4. *Earth Planet. Sci. Lett.* **243**, 504–519 (2006).
71. Rasmussen, T. L. & Thomsen, E. Warm Atlantic surface water inflow to the Nordic seas 34–10 calibrated ka B.P. *Paleoceanography* **23**, PA1201 (2008).
72. Rasmussen, T., Thomsen, E., Labeyriefi, L. & van Weering, T. C. E. Circulation changes in the Faeroe-Shetland Channel correlating with cold events during the last glacial period (58–10 ka). *Geology* **24**, 937–940 (1996).
73. Rasmussen, T., Thomsen, E., Troelstra, S. R., Kuijpers, A. & Prins, M. A. Millennial-scale glacial variability versus Holocene stability: changes in planktic and benthic foraminifera faunas and ocean circulation in the North Atlantic during the last 60,000 years. *Mar. Micropaleontol.* **47**, 143–176 (2002).
74. Rasmussen, T. L. et al. The Faroe-Shetland Gateway: Late Quaternary water mass exchange between the Nordic seas and the northeastern Atlantic. *Mar. Geol.* **188**, 165–192 (2002).
75. Kandiano, E. S., Bauch, H. A. & Müller, A. Sea surface temperature variability in the North Atlantic during the last two glacial-interglacial cycles: comparison of faunal, oxygen isotopic and Mg/Ca-derived records. *Palaeogeogr. Palaeoclimatol. Palaeoecol.* **204**, 145–164 (2004).
76. Kiefer, T., Sarnthein, M., Erlenkeuser, H., Grootes, P. M. & Roberts, A. P. North Pacific response to millennial-scale changes in ocean circulation over the last 60 kyr. *Paleoceanography* **16**, 179–189 (2001).
77. Harada, N. et al. Rapid fluctuation of alkenone temperature in the southwestern Okhotsk Sea during the past 120 ky. *Glob. Planet. Change* **53**, 29–46 (2006).
78. Martrat, B. et al. Four climate cycles of recurring deep and surface water destabilizations on the Iberian margin. *Science* **317**, 502–507 (2007).
79. Cacho, I., Grimalt, J. & Pelejero, C. Dansgaard-Oeschger and Heinrich event imprints in Alboran Sea paleotemperatures. *Paleoceanography* **14**, 698–705 (1999).
80. Hendy, I. & Kennett, J. Dansgaard-Oeschger cycles and the California Current System: planktonic foraminiferal response to rapid climate change in Santa Barbara Basin, Ocean Drilling Program hole 893A. *Paleoceanography* **15**, 30–42 (2000).
81. Sachs, J. P. & Lehmann, S. J. Subtropical North Atlantic temperatures 60,000 to 30,000 years ago. *Science* **286**, 756–759 (1999).
82. Simon, M. H. et al. Millennial-scale Agulhas current variability and its implications for salt-leakage through the Indian-Atlantic Ocean Gateway. *Earth Planet. Sci. Lett.* **383**, 101–112 (2013).
83. Lamy, F. et al. Antarctic timing of surface water changes off Chile and Patagonian ice sheet response. *Science* **304**, 1959–1962 (2004).
84. Pahnke, K., Zahn, R., Elderfield, H. & Schulz, M. 340,000 year centennial-scale marine record of southern hemisphere climatic oscillation. *Science* **301**, 948–952 (2003).
85. Caniupán, M. et al. Millennial-scale sea surface temperature and Patagonian Ice Sheet changes off southernmost Chile (53°S) over the past ~60 kyr. *Paleoceanography* **26**, PA3221 (2011).
86. Barbante, C. et al. One-to-one coupling of glacial climate variability in Greenland and Antarctica. *Nature* **444**, 195–198 (2006).
87. Augustin, L. et al. Eight glacial cycles from an Antarctic ice core. *Nature* **429**, 623–628 (2004).
88. Blunier, T. & Brook, E. J. Timing of millennial-scale climate change in Antarctica and Greenland during the Last Glacial period. *Science* **291**, 109–112 (2001).
89. Van Meerbeeck, C. J. et al. The nature of MIS 3 stadial-interstadial transitions in Europe: new insights from model-data comparisons. *Quat. Sci. Rev.* **30**, 3618–3637 (2011).
90. Müller, U. C. et al. The role of climate in the spread of modern humans into Europe. *Quat. Sci. Rev.* **30**, 273–279 (2011).
91. Wang, Y. J. et al. A high-resolution absolute-dated late Pleistocene Monsoon record from Hulu Cave, China. *Science* **294**, 2345–2348 (2001).
92. Bar-Matthews, M., Ayalon, A., Gilmour, M., Matthews, A. & Hawkesworth, J. C. Sea-land oxygen isotopic relationships from planktonic foraminifera and speleothems in the Eastern Mediterranean region and their implication for paleorainfall during interglacial intervals. *Geochim. Cosmochim. Acta* **67**, 3181–3199 (2003).
93. Grimm, E. C. et al. Evidence for warm wet Heinrich events in Florida. *Quat. Sci. Rev.* **25**, 2197–2211 (2006).
94. Yuan, D. et al. Timing, duration and transitions of the last interglacial Asian monsoon. *Science* **304**, 575–578 (2004).
95. Schulz, H., von Rad, U. & Erlenkeuser, H. Correlation between Arabian Sea and Greenland climate oscillations of the past 110,000 years. *Nature* **393**, 23–25 (1998).
96. Altabet, M., Higginson, M. & Murray, D. The effect of millennial-scale changes in Arabian Sea denitrication on atmospheric CO_2. *Nature* **764**, 159–162 (2002).
97. Hodell, D. A. et al. An 85-ka record of climate change in lowland Central America. *Quat. Sci. Rev.* **27**, 1152–1165 (2008).
98. Burns, S. J., Fleitmann, D., Matter, A., Kramers, J. & Al-Subbary, A. A. Indian Ocean climate and an absolute chronology over Dansgaard/Oeschger events 9 to 13. *Science* **301**, 1365–1367 (2003).
99. Peterson, L. C., Haug, G. H., Hughen, K. A. & Roehl, U. Rapid changes in the hydrologic cycle of the tropical Atlantic during the last glacial. *Science* **290**, 1947–1951 (2000).
100. Jennerjahn, T. C. et al. Asynchronous terrestrial and marine signals of climate change during Heinrich events. Science 306, 2236–2239 (2004).
101. Tierney, J. E. et al. Northern hemisphere controls on tropical southeast African climate during the past 60,000 years. *Science* **322**, 252–255 (2008).
102. Brown, E. T., Johnson, T. C., Scholz, C. A., Cohen, A. S. & King, J. W. Abrupt change in tropical African climate linked to the bipolar seesaw over the past 55,000 years. *Geophys. Res. Lett.* **34**, L20702 (2007).
103. Wang, X. et al. Wet periods in northeastern Brazil over the past 210 kyr linked to distant climate anomalies. *Nature* **432**, 740–743 (2004).
104. Kanner, L. C., Burns, S. J., Cheng, H. & Edwards, R. L. High-latitude forcing of the South American summer monsoon during the Last Glacial. *Science* **335**, 570–573 (2012).
105. Turney, C., Kershaw, A. & Clemens, S. Millennial and orbital variations of El Nino/Southern Oscillation and high-latitude climate in the Last Glacial period. *Nature* **428**, 306–310 (2004).
106. Baker, P. A. et al. Tropical climate changes at millennial and orbital timescales on the Bolivian Altiplano. *Nature* **409**, 698–701 (2001).
107. Cruz, F. W., Burns, S. J., Karmann, I., Sharp, W. D. & Vuille, M. Reconstruction of regional atmospheric circulation features during the late Pleistocene in subtropical Brazil from oxygen isotope composition of speleothems. *Earth Planet. Sci. Lett.* **248**, 495–507 (2006).
108. Wang, X. et al. Interhemispheric anti-phasing of rainfall during the Last Glacial period. *Quat. Sci. Rev.* **25**, 3391–3403 (2006).
109. Cruz, F. W. Jr et al. Insolation-driven changes in atmospheric circulation over the last 116000 years in subtropical Brazil. *Nature* **434**, 63–66 (2005).
110. Ziegler, M. et al. Development of Middle Stone Age innovation linked to rapid climate change. *Nat. Commun.* **4**, 1905 (2013).
111. Barker, S. et al. Interhemispheric Atlantic seesaw response during the last deglaciation. *Nature* **457**, 1097–1102 (2009).
112. Li, C., Battisti, D. S. & Bitz, C. M. Can North Atlantic sea ice anomalies account for Dansgaard-Oeschger climate signals?. *J. Clim.* **23**, 5457–5475 (2010).
113. Weber, S. L. et al. The modern and glacial overturning circulation in the Atlantic Ocean in PMIP coupled model simulations. *Clim. Past* **3**, 51–64 (2007).

Acknowledgements

We thank colleagues at the Alfred Wegener Institute Helmholtz Centre for Polar and Marine Research in Bremerhaven for maintaining the supercomputer. The study is supported by the Basic Science Center for Tibetan Plateau Earth System (BSCTPES, NSFC project no. 41988101), the Natural Science Foundation of China (no. 42075047) and the German Helmholtz Postdoc Program (PD-301). We also acknowledge financial support from UK NERC (grants nos. NE/J008133/1 and NE/L006405/1) to S.B. and the German BMBF funded project PalMod (01LP1504A, 01LP1915A and 01LP1916B) and the PACES programme of the AWI to G.K. and G.L. A sabbatical visit by R.D. to AWI was financially supported by the Faculty of Science at the University of Melbourne.

Author contributions

X.Z. conceived and developed the research, and wrote the manuscript with help of S.B. and G.K. All authors contributed to the final version of the manuscript.

Competing interests

The authors declare no competing interests.

Additional information

Extended data is available for this paper at https://doi.org/10.1038/s41561-021-00846-6.

Correspondence and requests for materials should be addressed to Xu Zhang.

Peer review information *Nature Geoscience* thanks Pepijn Bakker and Sophia Hines for their contribution to the peer review of this work. Primary Handling Editor(s): James Super.

Reprints and permissions information is available at www.nature.com/reprints.

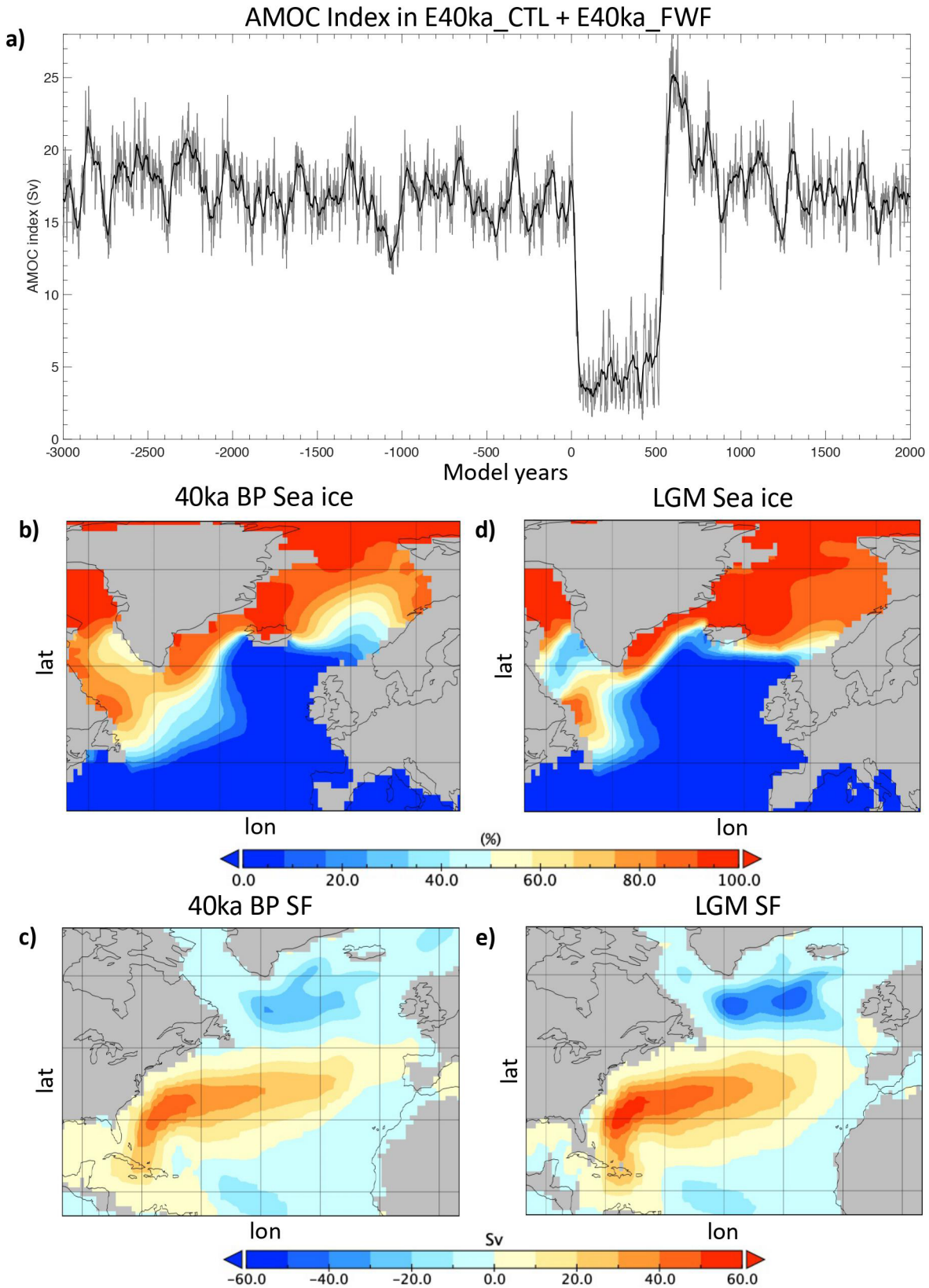

Extended Data Fig. 1 | Climate characteristics of E40ka_CTL control run. a, AMOC index in E40ka_CTL and its response to freshwater hosing (E40ka_FWF). The hosing lasts for 500 years, starting from the 0th year before which is the control experiment E40ka_CTL. **b, c** Mean annual SIC and barotropic stream function (SF, units: Sv) under 40ka BP conditions[57]. **d, e** same as b, c, but under the LGM boundary conditions (E40ka_CTL).

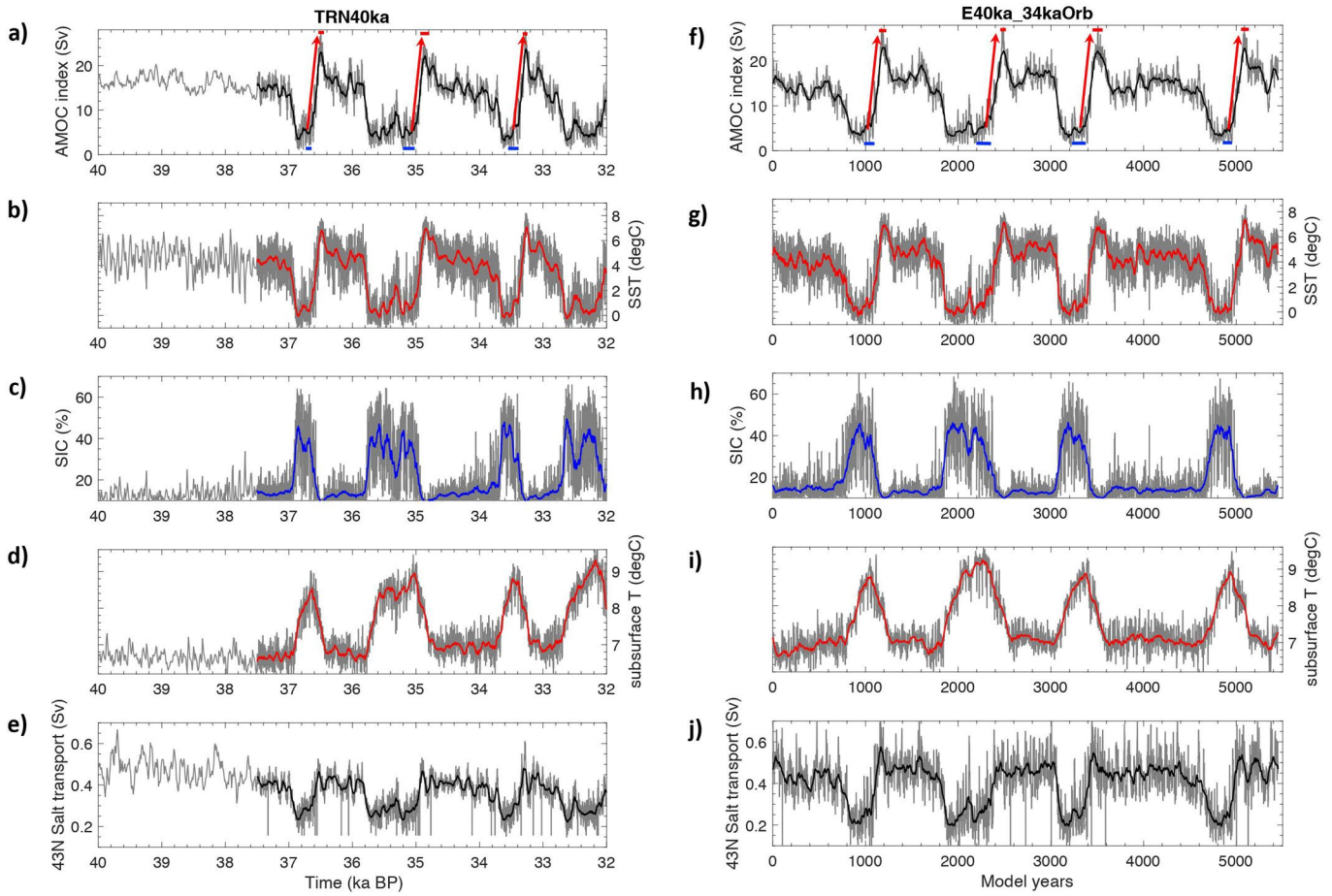

Extended Data Fig. 2 | Oscillating dynamics in the scenario with varying (a-e, TRN40ka) and constant (f-j, E40ka_34kaOrb) orbital configurations. **a)** and **e)** for AMOC index (units: Sv); **b)** and **g)** for sea surface temperature (units: °C), **c)** and **h)** for sea ice concentration (SIC, units: %), **d)** and **i)** for subsurface sea temperature (units: °C) in the key convection sites of the NA; **e)** and **j)** for meridional salt water transportation along 43°N (units: Sv) in the NA. We calculate the regional averages of SST, SIC and subsurface T in the northeastern NA (30°W-10°W, 50°-65°N). Bold lines show the 30-year running mean of the original data (thin grey lines). Bold lines show the 30-year running mean of the original data (thin grey lines). The short blue and red bold lines in (a) and (f) correspond to selected time intervals representing stadial and interstadial periods, respectively, which are used to calculate composite anomalies between strong and weak AMOC phases in Extended Data Fig. 3 and 7a, b. Note that length of these lines indicates length of time intervals.

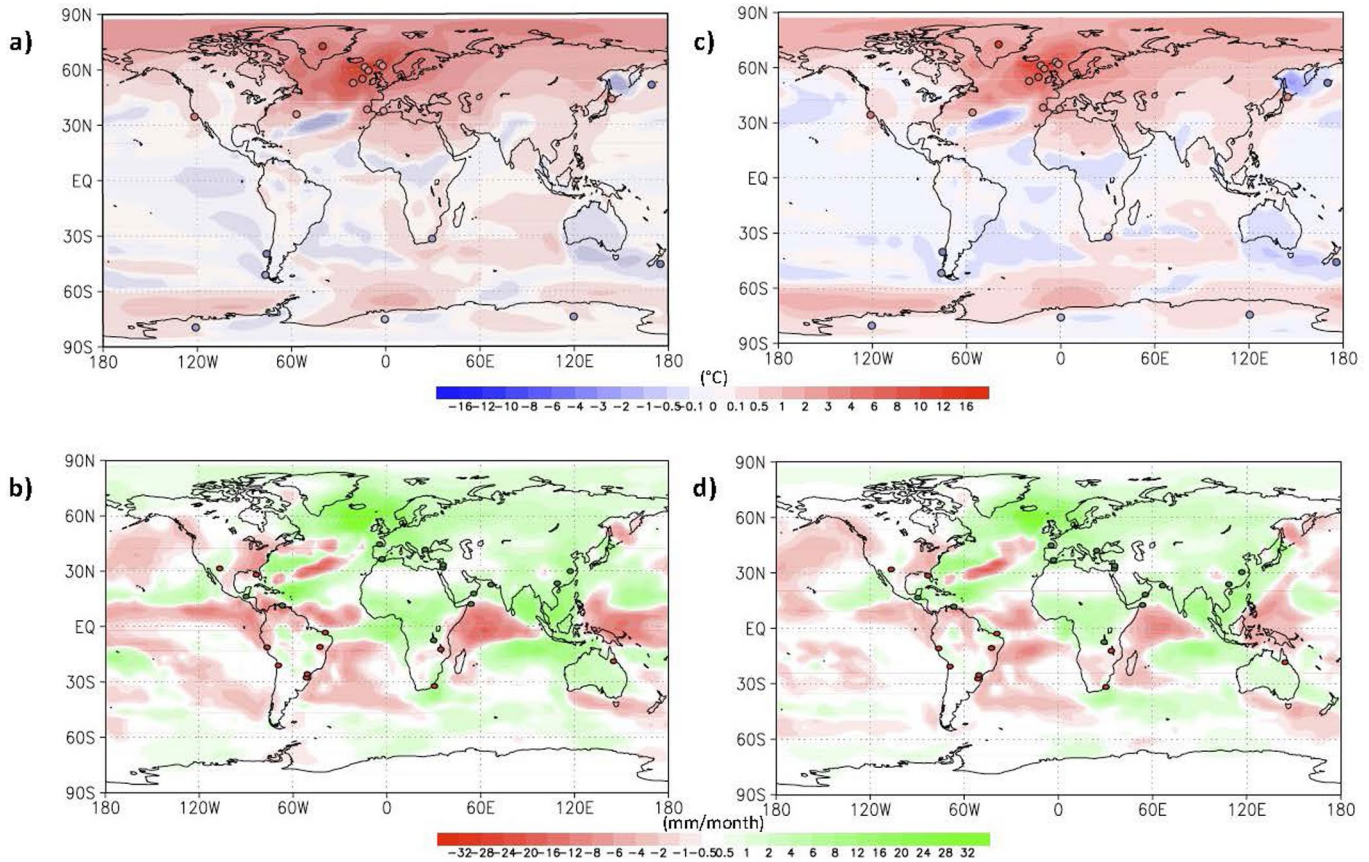

Extended Data Fig. 3 | Climate changes during stadial-to-interstadial transitions in TRN40ka (a-b) and E40ka_34kaOrb (c-d). a, b Composite surface temperature anomalies between simulated strong and weak AMOC phases as indicated by short red and blue bold lines in Extended Data Fig. 3a, f. **c, d**, same as (a) and (b), but for precipitation. The dots represent qualitatively the corresponding changes in paleoclimate proxy records as shown in Extended Data Table 2 and 3.

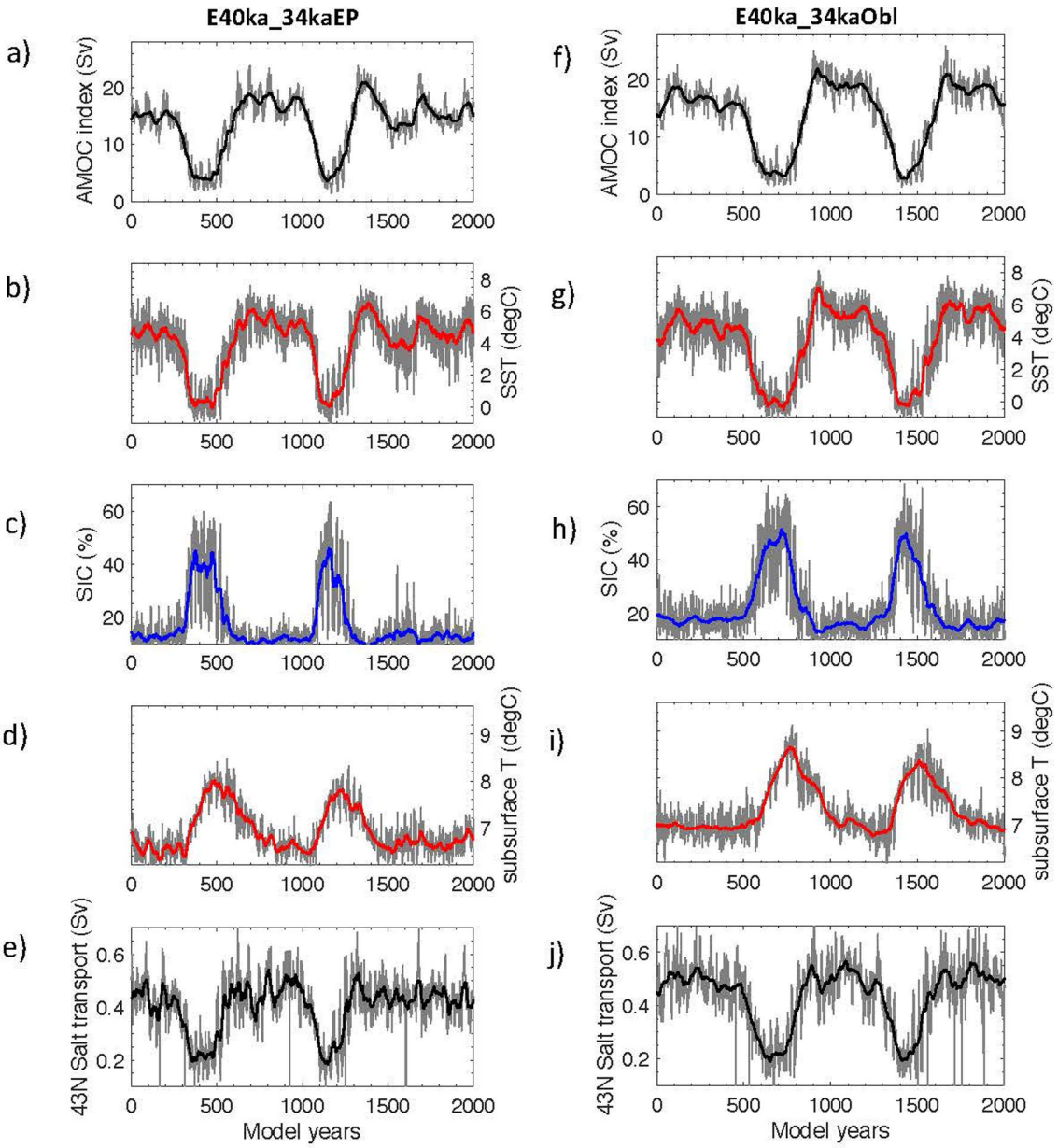

Extended Data Fig. 4 | Oscillating dynamics in the scenario with lowered eccentricity-modulated precession (a-e, E40ka_34kaEP) and obliquity (f-j, E40ka_34kaObl). a) and **e)** for AMOC index (units: Sv); **b)** and **g)** for sea surface temperature (units: °C), **c)** and **h)** for sea ice concentration (SIC, units: %), **d)** and **i)** for subsurface sea temperature (units: °C) in the key convection sites of the NA; **e)** and **j)** for meridional salt water transportation along 43°N (units: Sv) in the NA. We calculate the regional averages of SST, SIC and subsurface T in the northeastern NA (30°W-10°W, 50°-65°N). Bold lines show the 30-year running mean of the original data (thin grey lines).

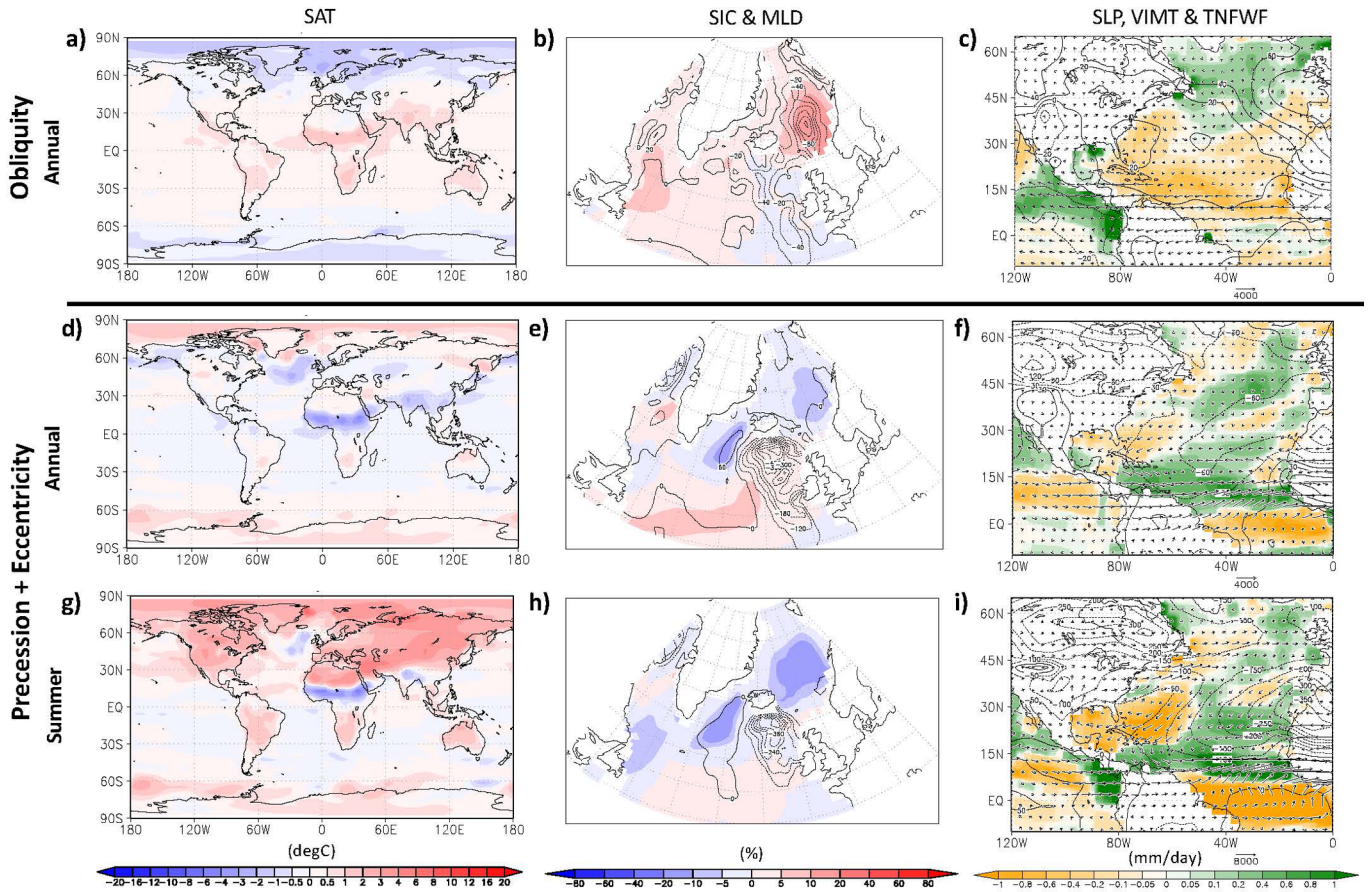

Extended Data Fig. 5 | Triggering dynamics regarding lowered obliquity (a-c, E40ka_34kaObl) or eccentricity-modulated precession (d-i, E40ka_34kaEP). a, b, c, Annual mean anomalies of surface air temperature (SAT, units: °C), SIC (shaded, units: %) and mixed layer depth (contour, units: m), and sea level pressure (SLP, contour, units: Pa), total net freshwater flux into the ocean (TNFWF, shaded, units: mm·day^{-1}) and vertical integrated moisture transport (VIMT, vector, units: kg·m^{-1}s^{-1}) between the 100-year average before the onset of its initial transition into a weak AMOC phase in E40ka_34kaObl and that in the control run E40ka_CTL; **d, e, f**, same as a, b, c, but for annual mean anomalies between 40-year average before the onset of its initial transition into a weak AMOC phase in E40ka_34kaEP and that in E40ka_CTL; **g, h, i**, same as d, e, f, but for boreal summer mean anomalies.

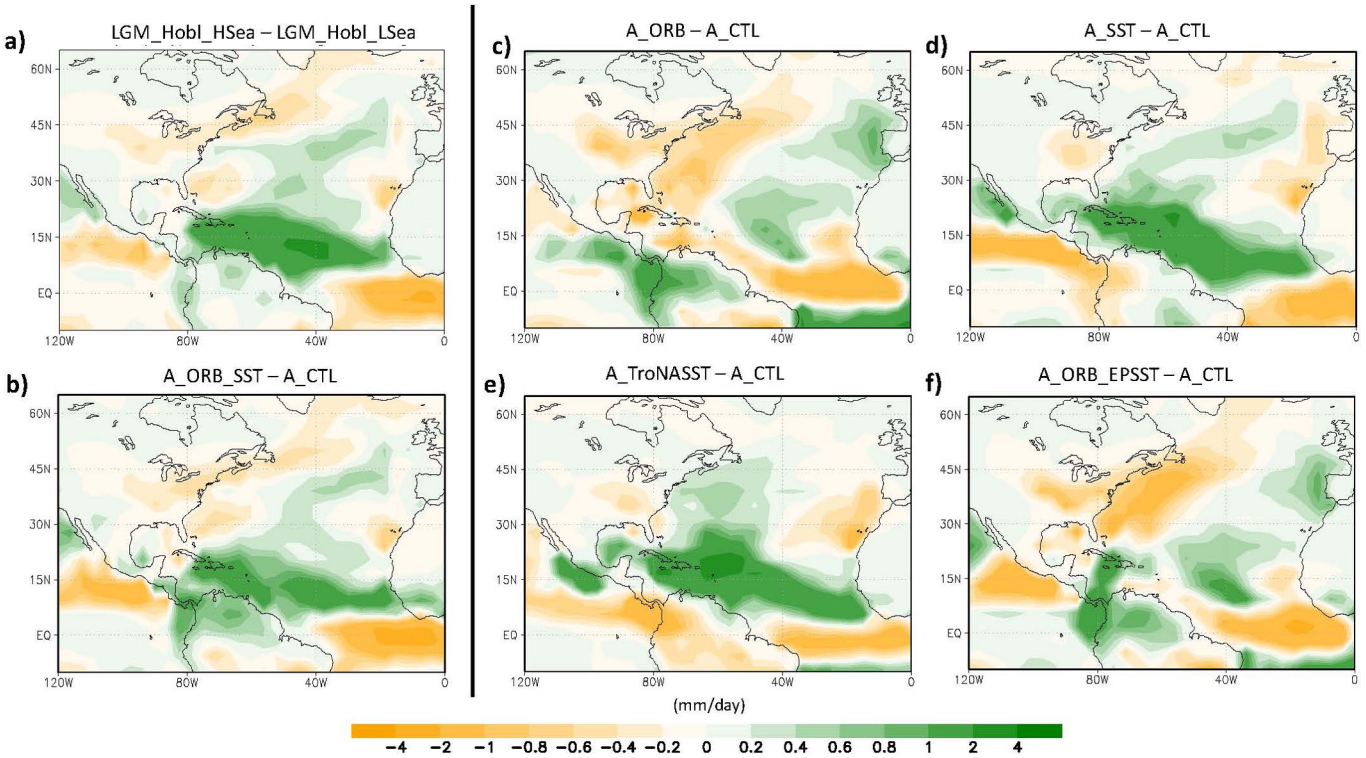

Extended Data Fig. 6 | Governing dynamics of precession-induced tropical NA hydroclimate changes. a. Mean annual precipitation anomaly between high and low boreal summer insolation scenarios under LGM conditions in coupled model COSMOS. **b – f**. Mean annual precipitation anomalies of AGCM sensitivity runs in contrast to the AGCM control run (Methods, Extended Data Table 1).

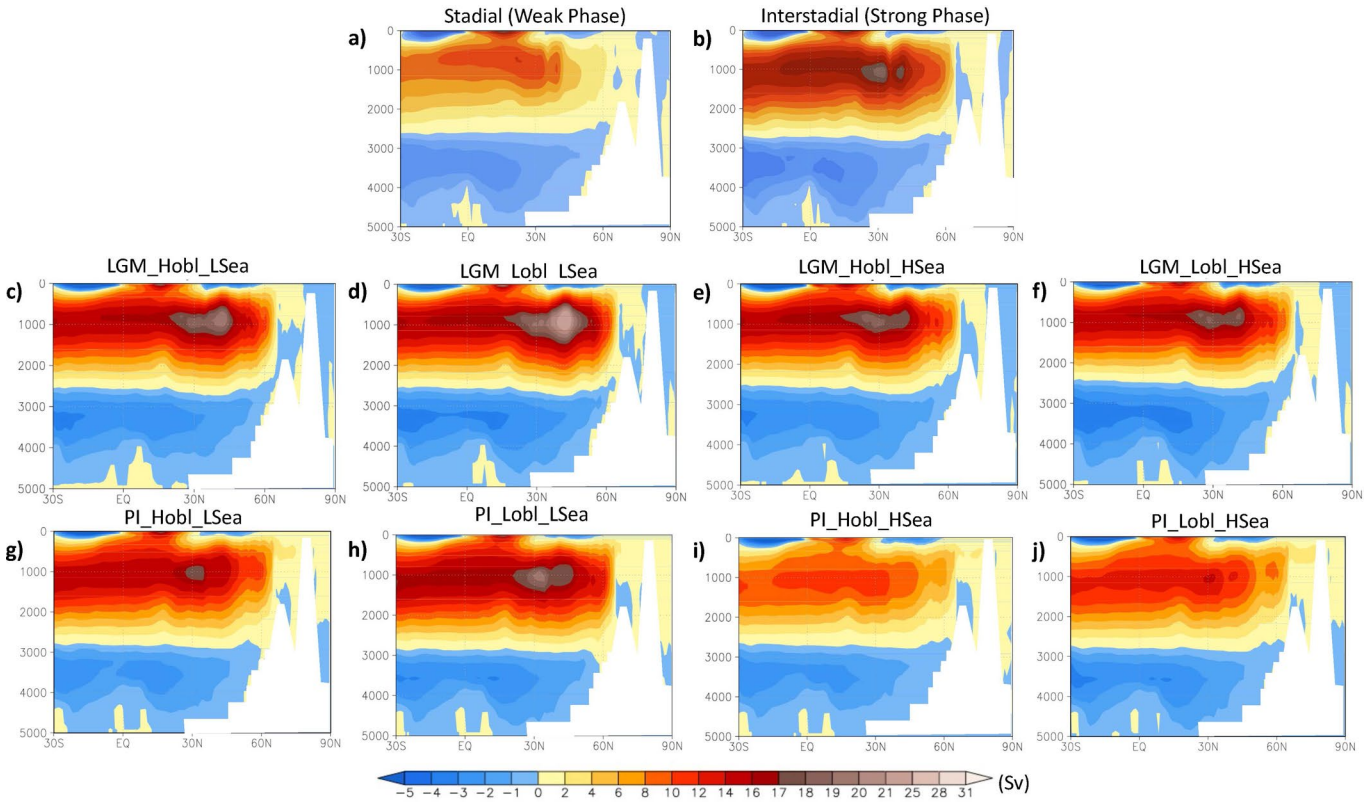

Extended Data Fig. 7 | Simulated AMOC states in the transient experiment under intermediate glacial conditions and equilibrium experiments under peak glacial and interglacial conditions. a, b AMOC states in the composited weak and strong phases of oscillatory regime in TRN40ka, representing stadial and interstadial AMOC state. **c, d, e, f** are equilibrated AMOC states in orbital sensitivity runs under the LGM conditions. **g, h, i, j** same as c-f but under the pre-industrial conditions.

Extended Data Table 1 | Model simulations in this study

COSMOS experiments

ID	Ecc.	Prec.	Obl.	Ice volume	Atm. CO_2	Initial state	Integrated years
Baseline experiments							
E40ka_CTL	0.013	358°	23.6°	40ka	195	PI[58]	5000
E40ka_FWF	0.013	358°	23.6°	40ka	195	E40ka_CTL	2500
Transient experiment							
TRN40ka	40ka to 32ka BP			40ka	195	E40ka_CTL	250+5500
Equilibrium experiments under intermediate glacial conditions							
Role of constant orbital settings							
E40ka_34kaOrb	0.015	84.84°	22.6°	40ka	195	E40ka_CTL	5000
E40ka_34kaObl	0.013	358°	22.6°	40ka	195	E40ka_CTL	2000
E40ka_34kaEP	0.015	84.84°	23.6°	40ka	195	E40ka_CTL	2000
Role of internal climate backgrounds							
E40ka_34kaOrb_nCO2	0.015	84.84°	22.6°	40ka	185	E40ka_34kaOrb	5400
E40ka_34kaOrb_pCO2	0.015	84.84°	22.6°	40ka	205	E40ka_34kaOrb	5400
E40ka_34kaOrb_50kaICE	0.015	84.84°	22.6°	50ka	195	E40ka_34kaOrb	3200
E40ka_50kaICE	0.013	358°	23.6°	50ka	195	E40ka_34kaOrb_50kaICE	5400
E50ka	0.013	229.6°	24.4°	50ka	204	E40ka_50kaICE	5400
Sensitivity experiments under peak glacial and interglacial conditions							
LGM_HObl_HSea	0.04	90°	24.5°	LGM	185	LGM[58]	1500
LGM_HObl_LSea	0.04	270°	24.5°	LGM	185	LGM[58]	1500
LGM_LObl_HSea	0.04	90°	22°	LGM	185	LGM[58]	1500
LGM_LObl_LSea	0.04	270°	22°	LGM	185	LGM[58]	1500
PI_HObl_HSea	0.04	90°	24.5°	PI	280	PI[58]	1500
PI_HObl_LSea	0.04	270°	24.5°	PI	280	PI[58]	1500
PI_LObl_HSea	0.04	90°	22°	PI	280	PI[58]	1500
PI_LObl_LSea	0.04	270°	22°	PI	280	PI[58]	1500

AGCM sensitivity runs

ID	Ecc.	Prec.	Obl.	Sea surface conditions	Regional forcing	50
A_CTL	0.04	270°	24.5°	LGM_Hobl_LSea	\	50
A_ORB_SST	0.04	90°	24.5°	LGM_Hobl_HSea	\	50
A_ORB	0.04	90°	24.5°	LGM_Hobl_LSea	\	50
A_SST	0.04	270°	24.5°	LGM_Hobl_HSea	\	50
A_ORB_EPSST	0.04	90°	24.5°	LGM_Hobl_LSea	Eastern Pacific SST is from *LGM_HObl_HSea*	50
A_TroNASST	0.04	270°	24.5°	LGM_Hobl_LSea	Tropical North Atlantic SST is from *LGM_HObl_HSea*	50

In the AGCM runs, "Eastern Pacific" is defined as the area in 25°S-25°N, 180°W-70°W of Pacific basin, "Atlantic" is defined as the Atlantic basin between 30°S and 60°N, and "tropical NA" is the area between 0° and 40°N of the NA basin.

Extended Data Table 2 | Temperature proxy data used for model-data comparison. Temperature proxy data used for model-data comparison

Nr.	Core ID	Lat.	Lon.	Response during S-IS transition	Approximate Range (degC)	Simulated Value (degC)	Proxy	Ref.
	Northern Hemisphere							
1	GISP2 ice core	72.6	-38.5	warming	~8-16	2.57	ice core	Grootes et al. 1993; Huber et al. 2006[69,70]
2	ENAM93-21	62.73	-3.88	warming	~1-3	1.84	planktic foraminifer assemblages	Rasmussen et al. 1996; Rasmussen and Thomsen 2008[71,72]
3	LINK 17	~61.3	-3	warming	~2-5	3.21	planktic foraminifer assemblages	Rasmussen and Thomsen 2008[71]
4	ENAM 33	61.26	-11.12	warming	~2-4	5.60	planktic foraminifer assemblages	Rasmussen et al. 2002; Rasmussen and Thomsen 2008[71,73]
5	DAPC-02	58.97	-9.62	warming	~3-5	5.61	planktic foraminifer assemblages	Rasmussen et al., 2002; Rasmussen and Thomsen 2008[71,74]
6	ODP 980	55.43	-14.7	warming	~4-6	4.88	planktic $\delta^{18}O$	McManus et al 1999[4]
7	M23414	53.537	-20.29	warming	~3-5	3.85	planktic foraminifer diversities	Kandiano et al. 2004[75]
8	ODP 883	51.2	167.77	cooling	~2.5-4	-0.14	planktic foraminifer assemblages	Kiefer et al. 2001[76]
9	MD01-2412	44.53	145	warming	~2-6	1.05	alkenone	Harada et al. 2006[77]
10	MD01-2444	37.6	-10.13	warming	~2-5	3.23	alkenone	Martrat et al. 2007[78]
11	MD95-2043	36.15	-2.62	warming	~1-3	2.05	alkenone/pollen	Cacho et al. 1999[79]
12	ODP 893a	34.29	-120.37	warming	~3-5	0.09	planktic foraminifer assemblages	Hendy and Kennett 2000[80]
13	MD95-2036	33.69	-57.57	warming	~2-5	0.57	alkenone	Sachs and Lehmen 1999[81]
	Southern Hemisphere							
14	CD154 17-17k	-33.32	29.47	cooling	~2	0.12	planktic foraminifer Mg/Ca	Simon et al., 2013[82]
15	ODP Site 1233	-41	-74.45	cooling	~2-3	-0.28	alkenone	Lamy et al 2004[83]
16	MD97-2120	-45.53	174.93	cooling	~2-3	-0.01	planktic foraminifer Mg/Ca	Pahnke et al 2003[84]
17	MD07-3128	-52.66	-75.57	cooling	~1-2	-0.30	alkenone	Caniupan et al 2011[85]
18	EDML ice core	-75	0	cooling	~0.5-3	-0.14	ice core	Barbante et al 2006[86]
19	Dome C ice core	-75.06	123	cooling	~1-3	-0.14	ice core	Augustin et al 2004[87]
20	Byrd ice core	-80	-129	cooling	~1-3	-0.14	ice core	Blunier and Brook, 2001[88]

Listed is the information regarding 20 temperature proxy records covering the period when atmospheric CO_2 is at varying intermediate levels (that is MIS3). Approximate range represents magnitudes of recorded temperature changes during transitions from cold stadials to warm interstadials, as documented in the corresponding literature. In this study, we use the intermediate level of reconstructed amplitudes for the model-data comparison (as shown in Extended Data Fig. 3a, c). For instance, if the proxy-recorded temperature fluctuation ranges between ~1-3 °C, we consider in our model-data comparison a conservative estimate of the reconstructed temperature fluctuation of ~2 °C.

Extended Data Table 3 | Information regarding 23 reconstructed precipitation records used for model-data comparison

Nr.	Core ID	Lat.	Lon.	Response during S-IS transition	Simulated Values (mm/mon)	Proxy	Ref.
	Northern Hemisphere						
21	MD01-2348	~44	~5	humid	3.9	Pollen	Van Meerbeeck et al. 2011[89]
22	Tenaghi Philippon core	40.97	24.22	humid	3.1	Terrestrial archive	Mueller et al. 2011[90]
23	Hulu Cave	32.5	119.17	humid	3.6	Stalagmite $\delta^{18}O$	Wang et al., 2001[91]
24	Peqiin Cave	32.58	35.19	humid	0.7	Cave speleothem $\delta^{18}O$	Bar-Matthews et al., 2003[92]
25	Soreq Cave	31.45	35.03	humid	0.6	Cave speleothem $\delta^{18}O$	Bar-Matthews et al., 2003[92]
26	Lake Tulane NAD27	27.59	-81.5	arid	0.6	Pollen and plant macrofossils	Grimm et al. 2006[93]
27	Dongge Cave	25.28	108.08	humid	1.7	Stalagmite $\delta^{18}O$	Yuan et al., 2004[94]
28	SO90-111KL/SO90-136KL	23.1	66.48	humid	0.9	Total organic carbon	Schulz et al. 1998[95]
29	RC27-23/RC27-14	18	57.65	humid	0.8	$\delta^{15}N$	Altabet et al. 2002[96]
30	Lake Peten Itza	16.92	-89.83	humid	1.2	Clay-gypsum	Hodell et al. 2008[97]
31	Socatra Island	12.5	54	humid	-1.2	Stalagmite $\delta^{18}O$	Burns et al. 2003[98]
32	ODP hole 1002C	10.71	-65.17	humid	-4.4	Ti/Fe ratio	Peterson et al. 2000[99]
	Southern Hemisphere						
33	GeoB3104-1/GeoB3912-1	-3.67	-37.72	arid	4.1	Fe/Ca ratio	Jennerjahn et al. 2004[100]
34	Lake Tanganyika	-6.7	29.83	humid	1.3	leaf wax δD	Tierney, J. E. et al. 2008[101]
35	Lake Malawi MAL05-2A	-10.02	34.19	arid	-0.4	lake sediment	Brown et al., 2007[102]
36	Northeastern Brazilian calcite speleothems	-10.17	-40.83	arid	-1.7	Speleothem and travertine deposit	Wang et al. 2004[103]
37	Pacupahuain Cave Stalagmite P09-PH2	-11.24	-75.82	arid	-1.1	Speleothem calcite $\delta^{18}O$	Kanner et al. 2012[104]
38	Lynch's crater	-17.62	146.17	arid	0.9	Degree of peat humification and ratio of sedges to grass	Turney et al. 2004[105]
39	Salar de Uyuni core	-20.23	-67.5	arid	-0.4	Natural r-rays	Baker et al. 2001[106]
40	Santana Cave Stalagmite St8	-24.53	-48.73	arid	2.4	Speleothem calcite $\delta^{18}O$	Cruz et al. 2006[107]
41	Caverna Botuvera Stalegmites	-27.22	-49.15	arid	0.1	Speleothem calcite $\delta^{18}O$	Wang et al., 2006[108]
42	Botuvera Cave Stalagmite Bt2	-27.22	-49.16	arid	0.1	Stalagmite $\delta^{18}O$	Cruz et al. 2005[109]
43	CD 154-17-17k	-33.27	29.12	arid	3.1	Fe/K ratio	Ziegler et al., 2013[110]

The records covering the period when atmospheric CO_2 is at varying intermediate levels (that is MIS3). Qualitatively reconstructed precipitation records are used to compare with simulated precipitation changes during stadial-to-interstadial transitions as shown in Extended Data Fig. 3b, d.